Geophys. J. Int. (2008) **173,** 249–264 doi: 10.1111/j.1365-246X.2007.03706.x

Moho depth and Poisson's ratio in the Western–Central Alps from receiver functions

D. Lombardi,[1] J. Braunmiller,[2] E. Kissling[1] and D. Giardini[1]

[1]*Institute of Geophysics, Swiss Federal Institute of Technology, ETH Hönggerberg,* CH-8093 *Zürich, Switzerland. E-mail: denis.lombardi@sed.ethz.ch*
[2]*College of Oceanic and Atmospheric Sciences, Oregon State University, Corvallis, USA*

Accepted 2007 November 30. Received 2007 September 15; in original form 2006 November 2

SUMMARY

Current knowledge about deep crustal structure of the Alpine orogen has mainly been derived from *P*-wave velocity models obtained from active and passive seismic experiments. A complementary *S*-wave model to provide lithological constraints necessary for unique structural interpretation has been missing to date. In this paper, we present important new information on *S*-wave velocity model in the Alps. We applied the receiver function method using 6 yr of high quality data from 61 permanent and temporary stations sampling the Western–Central Alps. We determined first-order crustal features Moho depth (H) and average Vp/Vs ratio (κ) with the H–κ stacking technique that uses timing of direct and multiple *P*-to-*S* converted phases from the Moho interface. Synthetic tests reveal a dipping Moho interface, expected beneath an orogen, causes a systematic bias of H and κ potentially leading to misinterpretation. We thus applied corrections determined from synthetic data to remove the bias, providing better fit of recovered Moho depths with active seismic estimates. For each site, we also obtained independent H and κ estimates based on the timing of the strong *Ps*-phase. Our results show a gently south–southeast dipping European Moho at a depth of ∼24–30 km beneath the Northern Alpine Foreland, steepening rapidly towards the Europe–Africa suture zone to reach a maximum depth of ∼55 km. South of the suture, the Moho of the Adriatic crust, promontory of the African plate, is at ∼35–45 km depth. In the previously ill-constrained Western Alps, we found the European Moho at ∼30 km depth beneath the more external units dipping east–northeast to reach ∼50–55 km in the inner core of the Alps. The Poisson's ratio clearly correlates with the tectonic units that comprise the Alps. Average crustal values in the European Alpine Foreland are close to 0.25. In the Alps, we observe low values (0.22) in the highly deformed nappes of the Mesozoic Helvetic and Southern Alps indicating a thickening of felsic upper-crustal material. In contrast, the Poisson's ratio is significantly higher (0.26) in the Penninic and Austroalpine units near the suture zone. This rapid and significant change marks a clear rupture between the Alpine forelands and the suture domain. We assign this high Poisson's ratio to doubling of mafic lower crust consistent with results from previous active seismic experiments. A continuation of the lower crustal wedge into the central part of the Western Alps, however, seems unlikely based on low observed Poisson's ratios.

Key words: Body waves; Continental tectonics: compressional; Crustal structure.

1 INTRODUCTION

1.1 Tectonic background

The Alps have been the focus of generations of geoscientists through decades and are now considered as a well-described geological object. This orogen is the result of subduction-collision processes involving the European plate and the Apulian (Adriatic) promontory of the African plate that occurred subsequently to the mid-Jurassic opening of the Central Atlantic Ocean. The sourthern margin of Europe (Helvetic nappes and Northern Foreland) and northern margin of Africa (Austroalpine and Southern Alps Units) converged asymmetrically in two main stages. A Cretaceous W–NW verging phase is preserved mainly in the Eastern Alps, while Tertiary NS to NW–SE convergence dominates surface exposures in the Western and Central Alps (Fig. 1). Remnants of the subducted intermediate terrain (Briançonnais Terrane) and basins (Valais and Ligurian or Alpine Tethys oceans) preserved in the Western–Central Alps are

© 2008 The Authors
Journal compilation © 2008 RAS

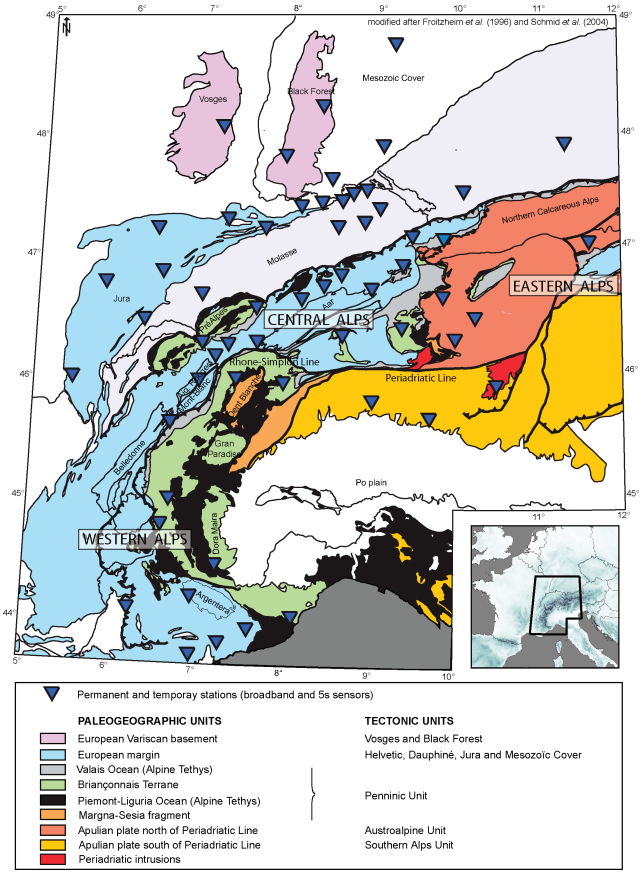

Figure 1. Map of the Western–Central Alps with main palaeogeographic units and corresponding tectonic units (modified after Froitzheim *et al.* 1996 and Schmid *et al.* 2004) and seismic stations (filled blue reversed triangles) used in this study. The lower-right-hand side inset indicates on a larger-scale topographic map the studied area by thick black lines.

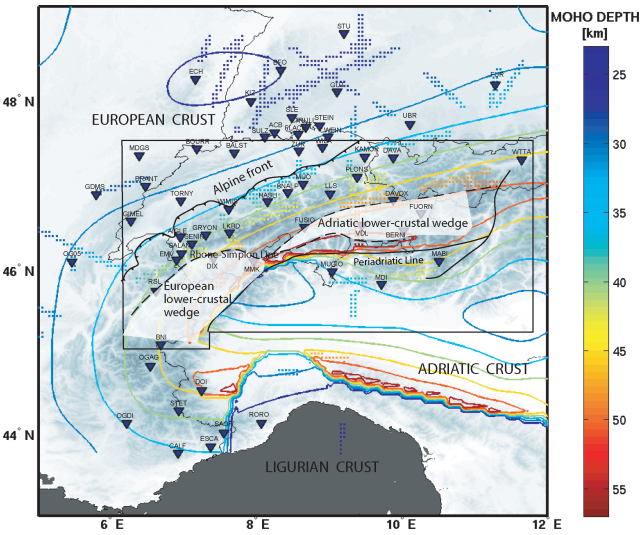

Figure 2. Moho depth contours in the Western–Central Alps and their forelands from the CSS model in 5-km increments (starting at 25 km) shown over greyscale topographic map. The dotted lines are locations of high-quality seismic profiles with uncertainties smaller than 5 km that provide the tightest constraint for the CSS model (Waldhauser *et al.* 1998). Filled blue reversed triangles denote seismic stations used. The semi-transparent white patches (limited by hatched line) show the location of the European and Adriatic lower-crustal wedges (redrawn after Fig. 5 of Schmid & Kissling 2000; the inner black frame indicates the limit of their figure). Also shown is the Insubric/Periadriatic line (solid line) that marks transitions from the foreland to the Penninic unit of the suture zone to the Southern Alps.

restricted to the so-called Penninic Unit. The latter also includes upper-crustal slices of both major continental plates. For a complete description of tectonic units in the Alpine region, we refer to Schmid *et al.* (2004).

1.2 Overview of the deep crustal Alpine structure

To unravel the dynamics of these complex tectonic processes, seismic methods that measure velocity changes reflecting contrasts in lithology are the main tools utilized by geophysicists. During the past several decades, in the framework of various European projects (ECORS-CROP, NFP20 and EGT), more than 200 reflection and refraction seismic profiles, primarily probing the Western–Central Alps, have been exploited with the aim of imaging the complexly deformed Alpine crust (see Roure *et al.* 1990a; Blundell *et al.* 1992; Pfiffner *et al.* 1997a for a non-exhaustive reference list). The crust–mantle interface, the Moho discontinuity, is a first-order velocity contrast and considerable effort has been placed to constrain its geometry. A compilation of the large data set of seismic profiles has been achieved by Baumann (1994) and later by Waldhauser *et al.* (1998) who elaborated a smoothly interpolated 3-D map of the Moho interface in the greater Alpine region (referred hereafter as 'CSS model', where 'CSS' stands for 'controlled-source seismology', see Fig. 2). Following the principle of being consistently as simple as possible, two vertical offsets were determined marking the limit of three different Moho. The European Moho subducting below an Adriatic Moho, which is further south, below the Apennines, overthrusted by the Ligurian Moho. The contact zone between these different crusts would occur in the southern part of the Western Alps close to the Ligurian Sea. Another major result was the detection of a major detachment between lower and upper crust of the European plate (Steck *et al.* 1997). The lower-crust subducts smoothly below the Alpine edifice, whereas the more buoyant upper crust, affected by intense deformation, is bending upward. This decoupling allows a large-scale wedge to protrude the European crust at depth corresponding to the top of lower-crust at approximately 30 km depth. This wedge is a key feature for a better understanding of continental collision processes, but mechanisms for its origin are still under discussion. The latest study from Schmid & Kissling (2000) reviewed previous interpretations established for the Western Alps (Bernoulli *et al.* 1990; Nicolas *et al.* 1990b; Roure *et al.* 1990b) and the Central Alps (Frei *et al.* 1989; Holliger & Kissling 1992; Schmid *et al.* 1996). Following Schmid *et al.* (1996) and Roure *et al.* (1996), they proposed the existence of a doubled European lower-crust in the Western Alps replaced to the east by the indentation of the Adriatic lower-crustal wedge, the transition between the two being rather abrupt and coincides with the Rhone-Simplon Line at the surface (see Fig. 2). The wedge in the Western Alps had previously been interpreted as lithospheric wedging of the Adriatic mantle based on gravity and seismic data (Bayer *et al.* 1989; Nicolas *et al.* 1990a), but local 3-D tomography (Solarino *et al.* 1997) clearly separates the up-tilted high-velocity Ivrea mantle material from the adjacent low-velocity wedge ruling out a mantle origin for the latter.

1.3 Towards a *Vs* model for the Alpine crust

Various crustal *Vp* models have been obtained from the active seismic experiments. Combined with more recent tomographic studies (Di Stefano *et al.* 1999; Paul *et al.* 2001; Waldhauser *et al.* 2002; Husen *et al.* 2003), they provide fairly well-constrained 3-D *Vp* models for the Western–Central Alps. Though, *P*-wave velocities alone are insufficient to assign a particular lithology, the complimentary information from shear waves, sampling rocks differently, is necessary to discriminate between the extreme varieties of crustal lithology (Christensen 1996). This information, however, is fairly rare in the Alpine region (Holbrook *et al.* 1988; Deichman & Rybach 1989; ECORS-CROP Deep Seismic Sounding Group 1989; Maurer & Ansorge 1992). Only few of the active seismic experiments included three-components sensors and explosions generally failed in generating strong shear energy (ECORS-CROP deep seismic sounding group 1989). More recent studies focused on determining *Vs* structure using passive seismic techniques still remain sparse (Bertrand & Deschamps 2000; Pedersen *et al.* 2003). The primary goal of our study is to determine first-order crustal features that are Moho depth and mean crustal *Vp*/*Vs* for the entire Western–Central Alps. Our results provide new insights about local Moho depth complementing the large-scale CSS model especially in areas without previous seismic control or where seismic profiles were of insufficient quality. We consider our main contribution resides in the first large-scale attempt in the whole Western–Central Alpine region to constrain *Vp*/*Vs* model that is of primary importance for lithologic interpretation and understanding of Alpine tectonic processes.

2 METHOD AND DATA

2.1 Receiver function technique

Detection of seismic phases converted at first-order seismic discontinuities is an efficient way to determine location and property of lithologies present in the Earth. The presence of microseismic and signal-generated noise in the *P*-wave coda, however, renders generally delicate identifications of such phases on raw seismograms. Amplitude from phase conversions can be enhanced from deconvolution of the vertical from the radial seismogram component. This technique referred as 'receiver function technique' has been developed (Phinney 1964; Burdick & Langston 1977; Langston 1977; Langston 1979; Ammon 1991) and successfully implemented in the frequency domain (Gurrola *et al.* 1994; Park & Levin 2000) as well as in time domain (Gurrola *et al.* 1995; Ligorria & Ammon 1999) and is widely used for structural studies from passive seismic experiments. Here, we implemented the iterative time domain deconvolution for its superior stability. Initiated by Ligorria & Ammon (1999) and based on the earlier work of Kikuchi & Kanamori (1982), this technique constructs receiver functions by minimizing the difference between the observed radial seismogram and the convolution of the iteratively updated Gaussian-sum time-series (the receiver functions) with the observed vertical seismogram. In addition to long-period stability, this technique also permits minimization of the through-like behaviour around the first *P* arrival usually observed when using frequency domain technique (due to limited bandwidth). For applications, we refer to Zor *et al.* (2003), Ozacar & Zandt (2004) and Dugda *et al.* (2005). In the Alpine region, the receiver function method has been applied at a local scale in the southwestern Alps (Bertrand & Deschamps 2000) and along 300-km-long array a 12° east as part of the TRANSALP experiment (Kummerow *et al.* 2004). Our study encompasses a much larger area covering the entire Western–Central Alps and its northern foreland using recordings from 61 stations (Figs 1 and 2).

2.2 Data

The bulk of our data set is composed of recordings from the 27 permanent broad-band stations of the Swiss Seismological Service (SDS-Net, see Fig. 2) covering the mid-1999 to end-of-2005 period; we also included eight stations with 5-s short-period sensors that provided stable receiver functions. For a network description see Baer *et al.* (2001). To increase the network aperture we installed seven temporary broad-band stations in the surroundings of the SDS-Net with online data access for a 2-yr duration. The stations in France and in Germany are within 90 km from the next SDS-Net site to maintain dense station spacing. Five sites were placed at existing short-period installations (RSL, OG05, KIZ, GUT and UBR) and two at new sites in the French Jura (MDGS and GDMS), see Fig. 2 for site location. To sample the entire Western–Central Alpine tectonic unit, we added data from permanent broad-band stations operating in countries surrounding Switzerland (Fig. 2). Data from stations BFO, BNI, CALF, DAVA, ESCA, FUR, OGDI, OGAG, SAOF, STET, STU and WTTA were extracted via AutoDRM requests (Kradolfer 1996), from ECH via NetDC requests (http://www.iris.edu/manuals/netdc/intro.htm) and from RORO via the RSNI network online database (http://mailserver1.dipteris.unige.it/geofisica/) and data from stations DOI, MABI and MDI are routinely transmitted to the SDS-Net by the INGV institute. Earthquake magnitude and epicentral distance were the criteria for selecting events. The threshold magnitude was set to 6.0 and 5.5 for earthquakes originating from the south to compensate for the lack of larger earthquakes from this source region. We selected data from teleseismic events in the 30–110° epicentral distance range. Usually events farther than 95° distance are not used for receiver function studies due to the insufficient amplitude of the P_{diff} phase. However, few acceptable receiver functions (less than 0.5 per cent of the data set) were produced for events usually larger than magnitude 7.0 and for receiver sites with strongly dipping Moho, thus providing a sufficient apparent incidence angle. Overall, from 1999 August to 2005 December, our event selection leads to a database of nearly 25 000 three-component seismograms. Data were low-passed at 1 Hz and receiver functions were computed using a time window of 80 s including about 20 s of pre-event noise. We employed simple signal-to-noise criteria to eliminate not-usable receiver functions and then inspected the remaining traces visually to select almost 4000 quality receiver functions from 61 stations for further analysis.

2.3 H–κ stacking technique

Due to their strong dependence on seismic velocities and depth of the crustal interfaces, receiver functions entail highly non-unique inverse problem (Ammon *et al.* 1990). Nevertheless, first-order crustal features, namely Moho depth and mean *Vp*/*Vs* ratio can be obtained from a straightforward technique under *a priori* assumption on *Vp* using relative traveltimes of the Moho converted *Ps* and reverberated *PpPs* and *PpSs* + *PsPs* phases (Zandt *et al.* 1995; eqs 2–4) which generally produce the largest amplitude in the receiver functions (Fig. 3). Zhu & Kanamori (2000) extended the method by introducing a formal grid search over Moho depth (H) and *Vp*/*Vs* (κ), the so-called H–κ stacking technique, transforming time domain receiver functions into the depth-*Vp*/*Vs* domain. The method sums the weighted receiver function amplitudes of the above mentioned

© 2008 The Authors, *GJI*, **173,** 249–264
Journal compilation © 2008 RAS

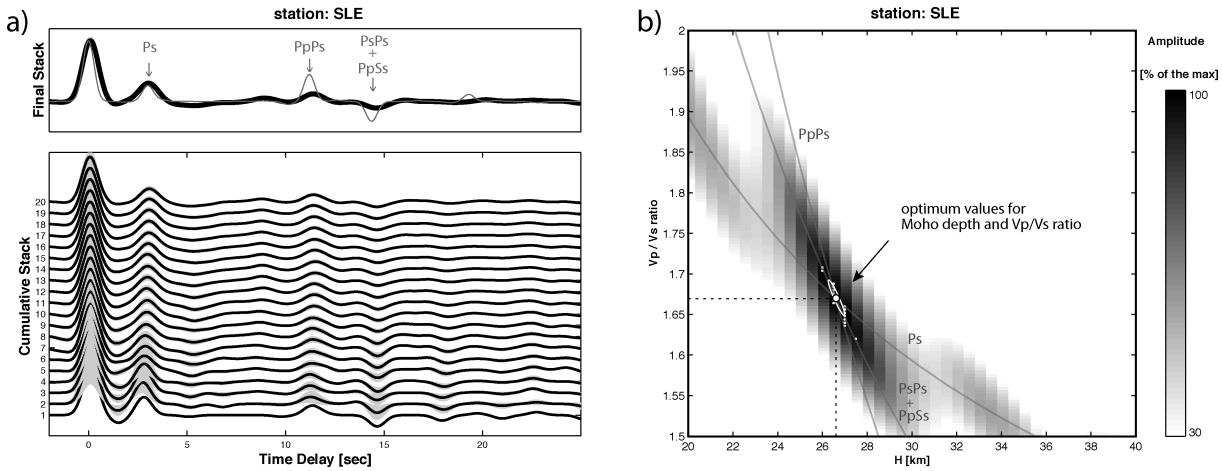

Figure 3. Receiver functions (a) and H–κ grid search analysis (b) for station SLE in northern Switzerland (Fig. 2). The cumulative stack is plotted from one (bottom) to 20 (top) receiver functions. Signal's 1σ standard deviation, shown in grey shading; decreases as the stack grows. Top shows the final stack of 73 receiver functions (thick black line) overlain by the synthetic receiver function (thin grey line) produced for the optimum Moho depth and Vp/Vs ratio from the H–κ grid search in (darkest colour in b) reflecting a coherent stack (eq. 1). Best model phase-arrival iso-time lines are shown as thin grey lines; move-out differences allow to constrain H and κ (b). Small white dots represent best-models for each bootstrap run with mean values and their associated 1σ standard deviations shown as large white dot and ellipse, respectively.

phases at the predicted arrival times for different pairs of crustal thickness (H) and Vp/Vs ratio (κ):

$$s(H,\kappa) = \sum_{i=1}^{n} [w_1 A_i(t_{Ps}) + w_2 A_i(t_{PpPs}) - w_3 A_i(t_{PpPs+PsPs})], \quad (1)$$

where w_1, w_2, w_3 are the weights associated with amplitude A of the Ps, $PpPs$ and $PpSs + PsPs$ phases, respectively. Summation is over the number of receiver functions n. The time delays t_{Ps}, t_{PpPs} and $t_{PpSs+PsPs}$ are related to crustal thickness, velocity and ray parameter p as follows:

$$H = \frac{t_{Ps}}{\sqrt{\kappa^2/V_P^2 - p^2} - \sqrt{1/V_P^2 - p^2}} \quad (2)$$

$$H = \frac{t_{PpPs}}{\sqrt{\kappa^2/V_P^2 - p^2} + \sqrt{1/V_P^2 - p^2}} \quad (3)$$

$$H = \frac{t_{PpPs+PsPs}}{2\sqrt{\kappa^2/V_P^2 - p^2}}. \quad (4)$$

The 'best' estimate for Moho depth H and Vp/Vs ratio κ beneath a station are obtained from the maximum of the summation (eq. 1), that is, for coherent amplitude stack of the direct and reverberated converted phases. Fig. 3 illustrates the stacking procedure and its results for station SLE in northern Switzerland (Fig. 2). We benefited from the 3-D crustal Vp model of Waldhauser *et al.* (2002) to introduce, in the computation, an appropriate *a priori* value on Vp for each station. During stacking, the amplitude of the Ps, $PpPs$ and $PsPs + PpSs$ phases were given equal weight (w_1, w_2 and w_3 of eq. 1) to ensure equal importance independent of their actual amplitude. This approach leads to better-constrained results, notably on Vp/Vs, compared to the weighting scheme proposed by Zhu & Kanamori (2000) who gave a large weight to the Ps phase (0.7-0.2-0.1), which already is the strongest phase on real data.

2.4 Uncertainty analysis

To estimate uncertainties on results from the H–κ stacking technique, we performed a bootstrap resampling technique for each station data set. We repeated the stacking procedure 200 times with a resampled data set that is a random replica of the original data set (see Efron & Tibshirani 1991 for principle, Chevrot & van der Hilst 2000; Julià & Mejía 2004 for applications with receiver functions) to obtain one standard deviation around the 'best' values illustrating the data variance (Fig. 3b). Some studies include uncertainty on *a priori Vp* within the H–κ and resampling analysis (Diehl *et al.* 2005; Dugda *et al.* 2005). However, receiver function traveltimes are relative to the direct P phase and a change in Vp will not affect significantly the Vp/Vs ratio but rather the result on Moho depth (Zhu & Kanamori 2000). The Vp/Vs ratio changes by less than 0.01 for a change of 0.1 km s^{-1} in Vp (Mohsen *et al.* 2005). Considering a reference Moho depth of 35 km and an uncertainty on average crustal Vp on the order of ± 0.2 km s^{-1}, results in about ± 1.5 km Moho depth uncertainty. In addition, one should be aware neither bootstrapping nor *a priori Vp* uncertainty considers the limited-band width of teleseismic data. The data frequency content implies phase arrival readings on the receiver function waveforms are accurate to 0.2–0.3 s limiting the resolution to about ± 2 km for Moho depth and about ± 0.03 for Vp/Vs. Therefore, the natural frequency content of the data is the major contributor to the global uncertainty of our results. Parameter uncertainties in Table 1 are the sum of uncertainties from bootstrap, Vp uncertainty and finite bandwidth considerations.

2.5 H–κ grid search and dipping Moho

2.5.1 Assumption in classical H–κ grid search

The H–κ technique does not require identification of individual phases. This is advantageous when analysing large data sets where the main phases are enhanced above noise level due to the stacking process and when the real crustal structure is close to the model used for traveltime calculations, usually a 1-D, horizontal, isotropic single

crustal layer over a half-space. Obviously, structural complications such as anisotropy (Levin & Park 1997), dipping Moho (Cassidy 1992) or simply presence of any other strong velocity contrast such as a sedimentary layer (Owens & Crosson 1988; Paulssen *et al.* 1993; Zelt & Ellis 1999) can seriously bias estimates of recovered Moho depth and Vp/Vs ratio.

2.5.2 Receiver functions in context of dipping Moho

In the Alps, other orogens or in subduction zone environments, the Moho interface is often dipping significantly presumably affecting timing of the converted phases and thus the optimum values yielded by the H–κ stack. To gain better insight into these effects, we produced synthetic receiver functions for dipping Moho using a ray theory-based code (Frederiksen & Bostock 2000). We built models composed of a single dipping crustal layer over an upper-mantle half-space systematically changing values for Moho depth, Moho dip and average Vp/Vs. All these models assume mean $Vp = 6.1$ km s^{-1} and a Moho interface dipping south, that is, towards backazimuth $= 180^\circ$. An example of synthetic receiver functions for a model with a 40 km deep Moho is shown in Fig. 4. Significant variations in time delay and amplitude as a function of backazimuth are observed particularly for the reverberated *PpPs* and *PsPs* + *PpSs* phases (Fig. 4 bottom). In the updip direction (backazimuth = 180°), because PpPs and *PsPs* + *PpSs* phases sample a wider area, they arrival later than those produced for a flat Moho. Combining the timing of the three phases, for this direction, would slightly overestimate depth and underestimate Vp/Vs ratio (Zandt *et al.* 1995). The opposite effect, but much stronger, is true for the downdip direction. However, considering the complete 360° backazimuth coverage, the multiple phases arrive earlier than the ones from the horizontal Moho model for most directions (Fig. 4 bottom) leading overall to an underestimate of H and overestimate of Vp/Vs. Also note that the resulting stack exhibits broad and weak multiple phases at earlier times (than a flat Moho) while the *Ps* phase remains undisturbed in time and amplitude (Fig. 4 top) suggesting simply stacking receiver functions over a wide azimuthal range to improve signal strength might not always produce desired results. Fig. 5 depicts the H–κ stack results for the model described in Fig. 4 for dominant *Ps* weighting (Fig. 5a) and for an equal-phase weighting (Fig. 5b). Moho depth and Vp/Vs estimates (dark shaded area) trade-off strongly in the first case (Fig. 5a) because of the dominance of *Ps* contributions and the weak incoherent 'stack' of the multiple phases (Fig. 4 top) with the parameter estimates spread over the *Ps* iso-line. The equal-phase weighting scheme we preferred constrains the parameters much tighter (small dark shaded area in Fig. 5b). The recovered parameters, however, are systematically biased towards shallower Moho depth and higher Vp/Vs ratio than true model parameters. We can correct for the systematic bias (see below).

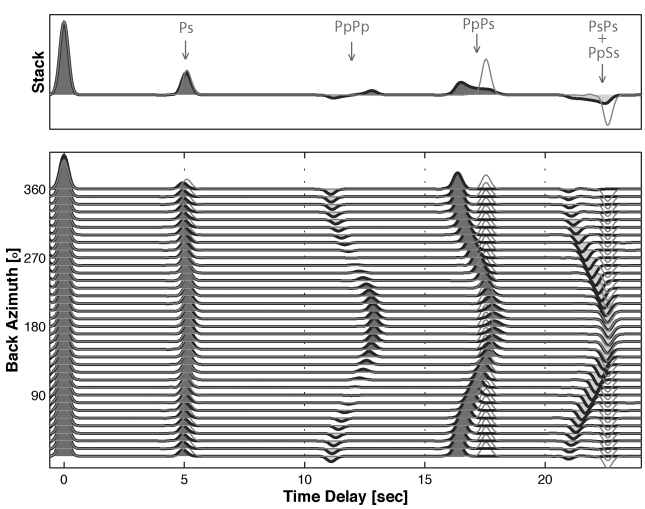

Figure 4. Synthetic receiver functions as function of backazimuth (bottom) and stack (top) for a model with Moho depth = 40 km, $Vp/Vs = 1.75$, $Vp = 6.1$ km s^{-1} and a Moho dip of 10°. The Moho dips towards backazimuth of 180°. Colour-filled traces are overlain by synthetics (thin grey line) for a horizontal Moho (dip = 0°). The *Ps* phase changes insignificantly with backazimuth. The *PpPp* phase near 12 s shows timing variations, changes polarity but has small amplitude; it is not observed for the horizontal model. The multiple phases *PpPs* and *PsPs* + *PpSs* show strong azimuthal variations in timing and amplitude. On the stack (top), these variations result in broader and weaker phases arriving earlier than for a horizontal model. Dip-induced early arrivals bias H–κ results towards shallower depth and higher Vp/Vs ratios (Fig. 5).

2.5.3 H–κ grid search for dipping Moho: general case

We calculated synthetic receiver functions for a dipping Moho-overhalf-space model systematically varying H, κ, the Moho dip and for even-spaced 360° backazimuth coverage to compile the apparent results for H and κ. We performed the analysis over a wide range of parameters to provide general results of use beyond the Alpine domain. The differences between the apparent results for H and κ and the true values are referred hereafter as 'error in Moho depth' and 'error in Vp/Vs'. We found that these errors have little dependence on each other; we thus only show error in Moho depth as function of true depth and Moho dip angle (Fig. 6) and error in Vp/Vs ratio as function of true Vp/Vs ratio and Moho dip angle (Fig. 7). For typical continental crust (Moho at 20–40 km depth and dip $\leq 5^\circ$), the Moho depth estimate from H–κ analysis is ≤ 1 km smaller than the true value (Fig. 6). For larger Moho depth and dip values, the error, however, becomes significant. For a Moho deeper than 40 km and dip exceeding 10°, characteristic of many orogens, the H–κ result underestimates the true value by at least 3 km (Fig. 6) exceeding 6 km for Moho-depths of 70–80 km as encountered in the Andean and Himalayan mountain belts. Results for the Vp/Vs ratio are even more telling, since already a 5° Moho dip results in a Vp/Vs ratio overestimation by 0.02 and for 10° reaches about 0.06 (Fig. 7). Such large differences, when not accounted for, could lead to a completely incorrect lithological interpretation underscoring the importance of considering dip-corrections when using the H–κ technique. It should be noted, the errors given here are representative of complete 360° backazimuth coverage and may change with particular region of the Earth considering regional dip direction and available data coverage.

2.5.4 H–k grid search for dipping Moho: our data set

Similarly, to estimate the possible errors generated by the use of H–κ grid search on our data set, we repeated the synthetic analysis for an average, non-even azimuthal coverage similar to our data coverage. We extracted local dip and dip-direction for each site from the CSS model and not from the receiver functions. As presented in Fig. 4, receiver functions for a dipping Moho show extreme time and waveform variations in the downdip and updip directions. Thus, it is crucial for the determination of the dip angle and dip direction that the data set sample these two opposite directions. We attempted to extract this information from azimuth-binned receiver functions at

© 2008 The Authors, *GJI*, **173,** 249–264
Journal compilation © 2008 RAS

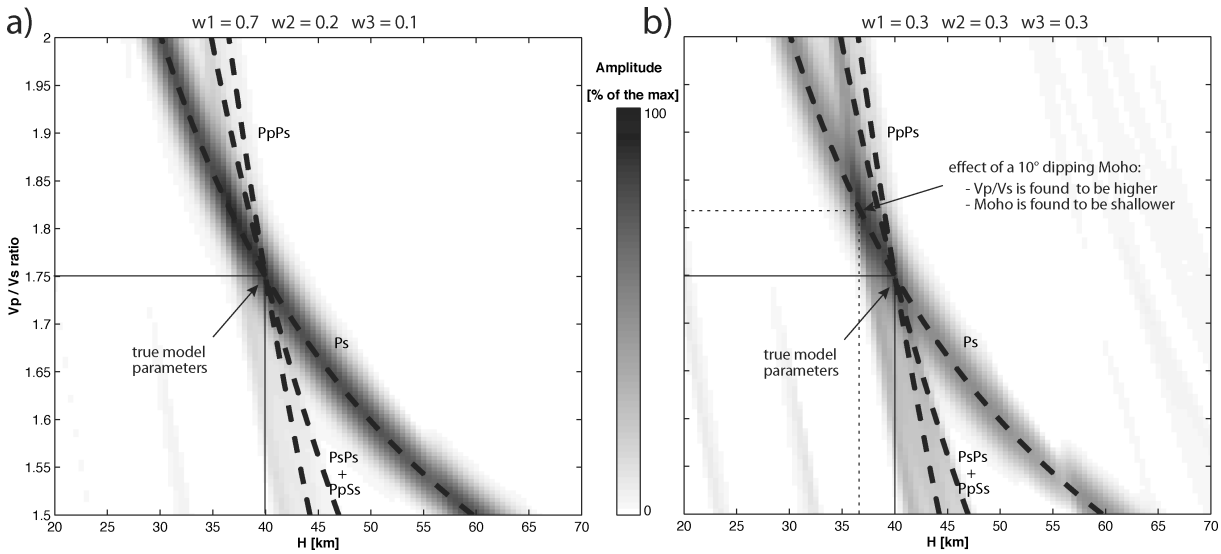

Figure 5. H–κ grid search for model described in Fig. 4 using amplitude weighting scheme proposed by Zhu & Kanamori (2000), that is, $w_1 = 0.7$, $w_2 = 0.2$ and $w_3 = 0.1$ (a) and scheme adopted here, that is, $w_1 = w_2 = w_3 = 0.3$ (b). Combination of a strong and stable *Ps* phase and a dominant weight (a) yields a spread of the largest amplitudes along the *Ps* line resulting in poorly resolved Moho depth and *Vp*/*Vs* ratio. For the weighting scheme adopted here (b), the compact high-amplitude region apparently defines Moho depth and *Vp*/*Vs* ratio tightly but is offset from the true model parameters (indicated by intersection of the flat-Moho iso-time lines). Due to general early arrival of the reverberated phases (Fig. 4), the recovered Moho depth and *Vp*/*Vs* are, 3 km shallower and 0.07 higher (dotted lines) than true values (solid lines).

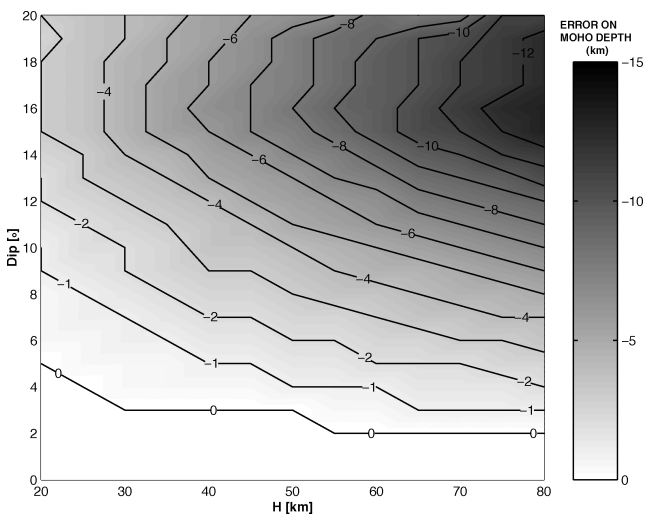

Figure 6. Error in Moho depth estimated from H–κ analysis for models with varying Moho thickness [20–80 km] and Moho dip angle [0–20°]. Plot is based on even 360° backazimuth range. We used $Vp = 6.1$ km s^{-1} and $Vp/Vs = 1.75$ for all models. Error surfaces for models with *Vp*/*Vs* from 1.65 to 1.85 are not significantly different. As expected, the error increases with increasing dip angle. For dips larger than 15°, the *Ps* phase dominates the H–κ stack over the weak multiples with strong azimuthal timing and amplitude variability leading to poorly constrained errors; for such cases, we strongly discourage the use of the H–κ method.

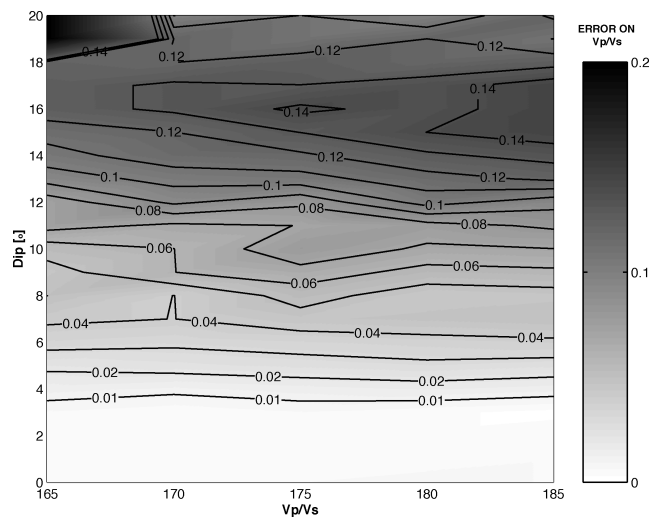

Figure 7. Error in *Vp*/*Vs* estimated from H–κ analysis for models with varying *Vp*/*Vs* ratio [1.65–1.85] and Moho dip angle [0–20°]. Plot is based on even 360° backazimuth range. We used $Vp = 6.1$ km s^{-1} and Moho depth = 40 km for all models. Errors for models with Moho depth from 20 to 80 km are not significantly different (not shown here). As expected, the error increases with increasing dip angle. As for Moho depth (Fig. 6), errors for large dips (>15°) are poorly resolved.

individual sites. Our data set, however, is dominated by events from a northerly backazimuth and only 3 per cent come from southern backazimuths (120–240°) corresponding to the updip direction for most sites. Lacking data from necessary backazimuths, we could not determine dip and dip-direction directly from our receiver function data set but we used, instead, the steepest gradient in the CSS Moho-model for each station. Since the CSS model is relatively smooth, it may not be the most accurate model locally and estimated dip direction and dip angle may deviate from the actual value with uncertainties difficult to estimate since no other study has provided this information at such large-scale. Bearing in mind unknown uncertainties on these parameters exist, we believe the effects of incorrect dip direction and dip angle may be minimized when binning numerous individual measurements to present general results. The resulting correction surfaces for Moho depth and *Vp*/*Vs* ratio are essentially the same as in Figs 6 and 7 and are not shown here. These corrections are small (<1 km and 0.015 for H and κ) in areas with flat (dip ≤5°) Moho, for example in the Variscan crystalline

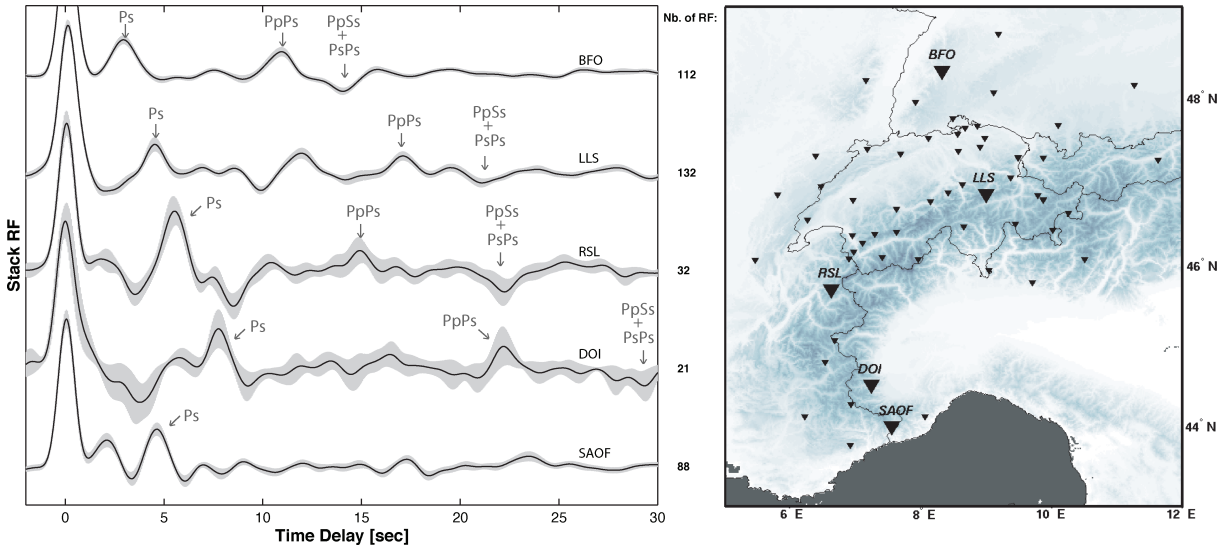

Figure 8. Examples of receiver function stacks (left-hand panel) for selected stations (right-hand panel). 'Nb. of RF' is number of receiver functions in stack. Stations BFO, LLS, RSL and DOI show clear *Ps* and multiple *PpPs* and *PsPs* + *PpSs* phases (labelled and indicated by thin arrows). Station SAOF does not show significant signal at times corresponding to multiples (∼10–30 s). However, the clear *Ps* phase at 4.7 s can be used to estimate Moho depth when combined with *a priori Vp*/*Vs*. Observed receiver function stacks for all stations are shown in supplemental Fig. S1.

massifs and Mesozoic cover of the northern Alpine foreland and moderate (∼1.5 km and 0.025) in the Molasse Basin with Moho dip ∼6°. In the Central and Western Alps, with crustal thickness [40–55 km] and average Moho dip [7–14°], corrections are critical reaching [2–7 km] for depth and [0.034–0.10] for *Vp*/*Vs* ratio. We performed the *H*–κ grid search to all 61 stations and checked the result by converting each station's depth-*Vp*/*Vs* pair to *Ps*, *PpPs* and *PsPs* + *PpSS* delay times and visually inspecting the receiver function amplitudes associated with these delay times. We obtained reliable (but dip-biased) *H* and κ estimates for 39 stations. As an example, we show receiver function stacks for selected stations in Fig. 8 (receiver function stacks for all stations are shown in the Supplementary material Fig. S1) with increasing complexity or loss of definition of later phases; for the top four stations we obtained reliable *H*–κ estimates. We used the correction surfaces (Figs 6 and 7) to correct for dip beneath each site and list resulting *H* and κ values and uncertainties in Table 1.

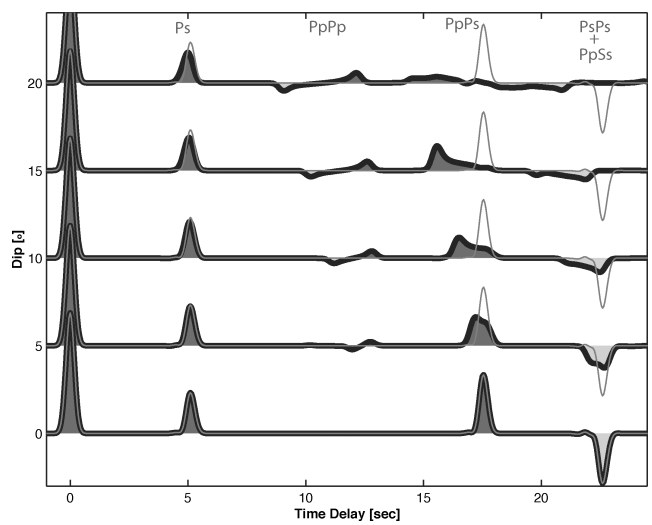

Figure 9. Synthetic receiver function stack as a function of Moho dip angle. The model is described in Fig. 4 with dip angle in the range [0–20°]. Time and amplitude of the stacked *Ps* phase is negligibly affected by the significant dip change. The stack of the multiple *PpPs* and *PsPs* + *PpSs* phases, though, is destructive impeding *Vp*/*Vs* estimation for dips larger than ∼15°.

2.6 Constraints on Moho depth from *Ps* times only

We could not obtain reliable *H*–κ estimates for 22 stations; most of them located near the Alpine suture zone where complex crustal structure generates complex receiver functions impeding identification of reverberated phases. As an example, Fig. 8 shows the stacked receiver function for SAOF characterized by a lack of reverberated signal but a strong *Ps* arrival. Indeed, synthetics show the *Ps* phase is stable in amplitude and arrival time even for Moho dip exceeding 10° (Fig. 9). Its arrival time, for example, differs by less than 0.1 s between a horizontal and a 15° dipping Moho. Combined with a reference *Vp*/*Vs* (and average slowness *p*), the *Ps* delay time leads directly to Moho depth (eq. 2). For each site, the *Ps* arrival, generally being the largest amplitude in the range 3–7 s, was handpicked on the stacked receiver function. The drawback of this simple approach is that *Vp*/*Vs* ratio inaccuracies map directly onto depth, for example, a (realistic) *Vp*/*Vs* uncertainty of ±0.1 leads to large ±5 km depth uncertainty for a 35-km-deep Moho with uncertainty increasing with Moho depth. For areas with little or controversial information about crustal thickness, such as the Western Alps where the CSS model is based on low quality data and interpolates over large data gaps (Fig. 2), it is worthwhile to estimate Moho depth from *Ps* arrivals even considering large inherent uncertainties of this approach. We obtained Moho depth estimates for 57 (of 61) stations from *Ps*-times using a *Vp*/*Vs* ratio of 1.75 and with depth uncertainties based on a conservative, broad range of *Vp*/*Vs* ratios [1.65–1.85]. For 18 stations, this approach provides Moho estimates consistent with CSS-model estimates (Table 1). For four sites, we could not obtain a Moho estimate, either due to lack of quality receiver functions (GDMS, UBR) or complex receiver functions without distinct *Ps* arrival (SALAN, FUSIO).

© 2008 The Authors, *GJI*, **173,** 249–264
Journal compilation © 2008 RAS

2.7 *Vp*/*Vs* ratio constraints from combined *Ps* time and CSS Moho model

The *Ps* arrival times, combined with independent Moho depths from the CSS model, provide an alternative to the *H*–*κ* method for obtaining crustal average *Vp*/*Vs* ratios (eq. 2) with the advantage of not relying on the weak reverberated phases notably close to the suture zone where they are hardly identifiable. Uncertainties in this approach are mainly due to uncertainties in CSS Moho depth, which is ±3 km in the best case (Baumann 1994; Waldhauser *et al.* 1998). However for some regions, these depth estimates are based mainly on the smooth interpolation process due to lack of data as for instance in the Western Alps. As slightly optimistic uncertainty estimate, we used the smallest uncertainty assigned to the closest seismic profile used for creation of the CSS model (see Waldhauser *et al.* 1998). The smallest resulting *Vp*/*Vs* uncertainty is about ±0.05. This approach provided 57 (of 61) additional *Vp*/*Vs* ratio estimates.

3 RESULTS AND DISCUSSION

Table 1 contains the results for Moho depth *H* and *Vp*/*Vs* ratio *κ* from *H*–*κ* analysis after dip-correction for 39 stations with reliably identified reverberated phases. About 20 per cent of these stations required significant dip-corrections of at least 3 km for depth and at least −0.06 for *Vp*/*Vs*. Table 1 also provides depth for additional 18 stations from the timing of the *Ps* phase, and *κ* for all 57 stations with identifiable *Ps* phase. For comparison, we also list the CSS Moho depth. The supplemental Fig. S1 shows the stacked receiver functions for 57 stations providing results.

3.1 Results for Moho depth

Moho depth from dip-corrected *H*–*κ* results range from 23 to 53 km (Fig. 10, inverted triangles) with a deepening from the northern Alpine foreland towards the SE until the Adriatic Moho, with Moho

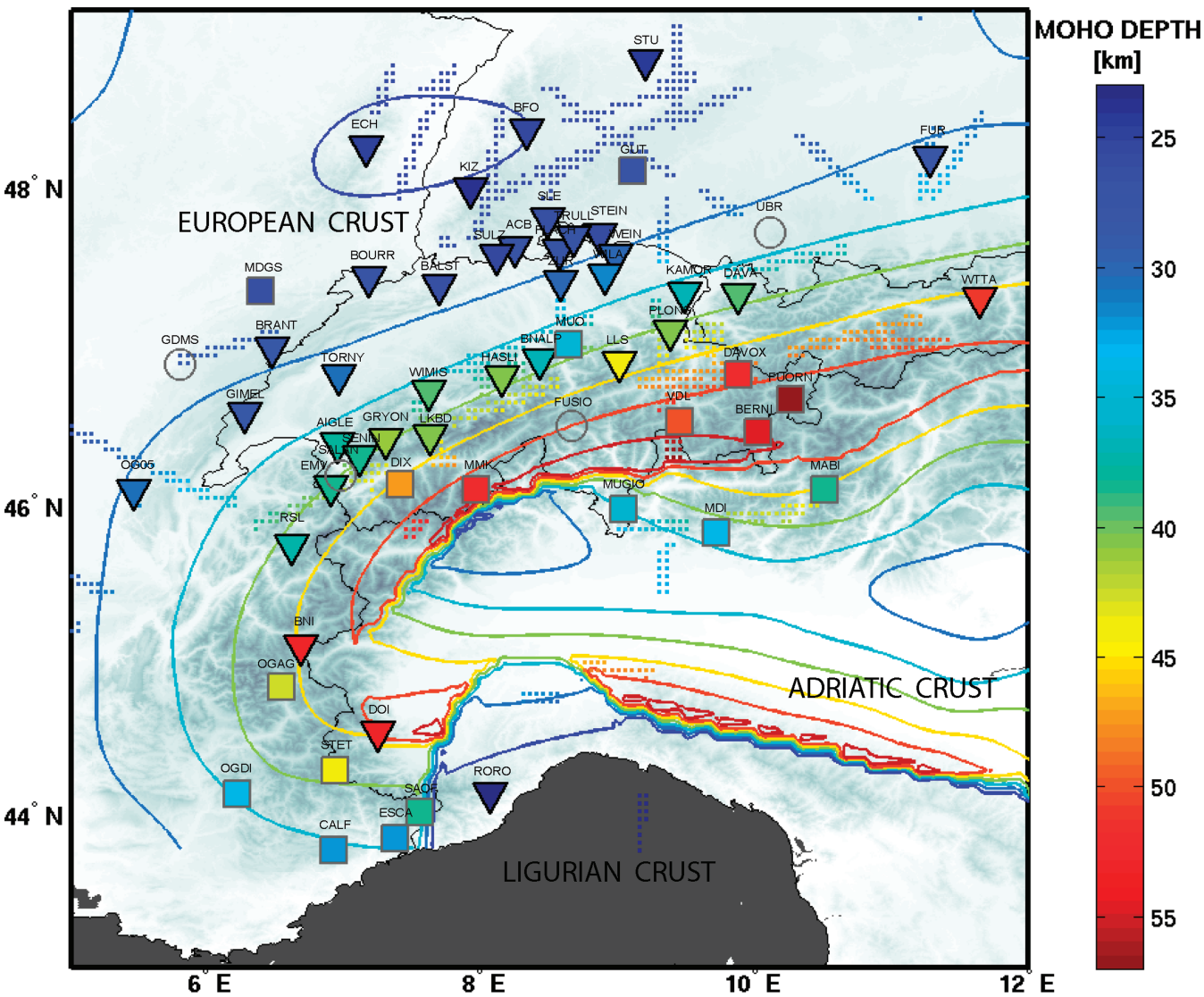

Figure 10. Moho depth variation in the Western–Central Alps and forelands. Reverse triangles represent Moho depth from *H*–*κ* analysis, squares depth from *Ps* times and *Vp*/*Vs* = 1.75. Stations without reliably identifiable *Ps* phase are shown as open circles. The symbols overlay Moho depth isolines and high-quality seismic profiles (dotted lines) with associated uncertainties smaller than 5 km from the CSS model. In the Central Alps, results from our study (symbols) are rather consistent with those from active seismic experiments and new estimates are provided for the Western Alps where the CSS model lacks high-quality data.

depth near 35 km, is reached south of the Insubric Line. Receiver functions for the deepest part of the European crust in the Central Alps (reaching almost 60 km thickness in the transition to the eastern Alps), as well as south of the Insubric Line and for sites in the Western Alps are complex and Moho depths are usually derived from *Ps* arrival times only (Fig. 10, squares). The dip-corrections, on average +2.6 km, brought H–κ depths closer to the CSS model, suggesting that such corrections are required for a dipping Moho environment**.** The mean uncertainty for H–κ and *Ps*-derived depths is about ±4 and ±5 km, respectively, yielding comparable resolution with the CSS model (nominally ±3 km, Baumann 1994). While receiver functions highlight local Moho depth, the CSS model reflects the geometrically simplest interface configuration considering it a smooth continuous surface. Both approaches yield consistent results (Fig. 10 and Table 1) implying local Moho measurements support the concept of a continuous, smooth Moho surface at least for areas with well-constrained receiver function results, that is, in the Alpine foreland and Prealps. Within the suture area, complex crust precludes accurate Moho depth estimates. However, additional measurements are provided in places where the CSS model lacks sufficient data, notably in the Western Alps (Fig. 10).

3.1.1 Moho in Western Alps

In the Western Alps, the CSS model provides Moho depths of about 35–45 km (Fig. 10). However, no high-quality seismic profile was available in the region and contours are constrained by interpolation. Other studies exist but lead to contradictory results about crustal thickness, we thus compare our results with the most recent study of Thouvenot *et al.* (2007; depth marked by a cross in Table 1). Receiver functions for most sites exhibit rather complex waveforms with no clear reverberated phases. Thus, our Moho depth estimates are mainly based on *Ps*-arrival times assuming a Vp/Vs of 1.75 ± 0.1. For stations CALF, ESCA, OGDI, SAOF, STET and OGAG, we obtain Moho depths of 31 ± 4, 30 ± 4, 37 ± 5, 37 ± 5, 44 ± 6 and 43 ± 6 km, respectively (Fig. 10 and Table 1). A Poisson's ratio larger than 0.30 ($Vp/Vs = 1.90$) is required to lower depths to 29 km at STET and to 19 km for CALF, ESCA and SAOF, depths inferred from receiver function forward modelling (Bertrand & Deschamps 2000). Considering Bertrand & Deschamps (2000) used a $Vp/Vs = 1.73$, their shallow Moho depths are probably an artefact due to a small data set that likely also affected their four-layer forward modelling results for crustal structure. A high Poisson's ratio of 0.30 is actually observed for DOI located further to the East but seems unlikely for these stations in the southwestern French Alps, too distant from the influence of the ultramafic Ivrea body. Our study thus suggests the European Moho in the Western Alps deepens from about 30–35 km in the Prealps to about 43–44 km near in the Argentera massif (STET) and in the vicinity of the Briançonnais (OGAG) to reach about 53 km thickness in the more internal units (BNI and DOI), values consistent with early (Giese & Prodehl 1977) and latest work (Thouvenot *et al.* 2007).

3.1.2 Receiver function profile in the eastern Central Alps

By contrast, the Central Alps are sampled by high-quality seismic profiles and densely spaced stations that provide a well-resolved Moho interface. With dense station spacing we can perform common conversion point (CCP) stacking (Dueker & Sheehan 1997) to obtain a continuous 2-D crustal cross-section from *Ps* conversion (for applications see Kind *et al.* 2002; Vergne *et al.* 2002; Gilbert & Sheehan 2004; Wittlinger *et al.* 2004; Gilbert *et al.* 2006). The CCP stacking accounts for the 5–10 km lateral offset of the Moho *Ps* conversions relative to a site location with offset depending on incidence angle, velocity structure and Moho depth, to allow binning signal recorded by different sites but generated at the same depth location. This procedure is often used to reduce noise and to enhance main features such as signal generated from the Moho interface. Given our station spacing of about 40 km, we can realize such a CCP stack perpendicular to the strike of the Alps only in the eastern Central Alps crossing from NE to SW (lower-left-hand side inset of Fig. 11) where the station spacing is the densest. We determined the location of *Ps* conversion points using Moho depth and Vp/Vs ratios from this study, mean crustal Vp from Waldhauer *et al*. (2002), and Moho dip angles as described in Section 2.5.4 and traced signal amplitude along the incoming converted *S*-wave ray path. Signal amplitudes are projected onto the profile and then binned for each time–distance with a horizontal grid space of 4 km with 2 km overlap. As a trade-off between the influence of possible out of plane reflections and the number of data, we used data from earthquakes with backazimuth differing by less than ±60° from the azimuth of the profile. As documented by Cassidy (1992), a dipping Moho influences not only the amplitude (Figs 4 and 9) but also the location of *Ps* conversion points relative to a recording site. For reverberated phases the horizontal distance change can be large, but for the *Ps* phase it is relatively small. For example, we calculated that a *Ps* phase generated by a *P* phase with incidence angle 23° relative to vertical impinging on a 10° dipping Moho interface at 45 km depth is only about 4 km horizontally away from the location predicted for a flat Moho for both, up- and downdip, directions. For other directions the effect is less. Given the grid space used, that is, 4 km, the figure presented here (Fig. 11) does not differ from a figure produced using flat Moho (not shown here). Also the use of constant $Vp/Vs = 1.73$ and CSS depth produced a similar picture (not shown here). Fig. 11 shows the large-scale crustal collision geometry in the eastern Central Alps that agrees well with the similarly located EGT profile (Ye *et al.* 1995). A relatively flat Moho at 25–30 km depth is imaged beneath the Variscan basement and Tabular Jura in southwest Germany (x = 0–100 km). From the Molasse Basin (x = 125 km) to the Austroalpine units (x = 250 km), the European Moho dip increases from gentle 5° to about 15°. Moho deepening is associated with a thickening of upper-crustal nappes that reach down to about 20 km depth. Although the image of the suture zone (x = 300 km) is less clear, a distinct offset in the continuity of the SE dipping European Moho, beneath the surface location of the Insubric Line (or Periadriatic Line), marks the transition to the possibly NE dipping Adriatic Moho. Two previously not-identified SE dipping segments (long dashes), one beneath the suture at 60–75 km depth (x = 250–280 km) and one beneath the Adriatic Moho (x = 320–420 km) at 50–55 km depth, could represent slivers of detached European lower-crust or remnants of a previous European Moho interfaces; the steep segment is only very tentatively identified. Also, only two stations sample each area and additional data are required to constrain existence, geometry and tectonic function of these potentially important features. A small-amplitude, but intriguing feature (hatched line) near x = 260 km just above the European Moho at 35–40 km depth, may be related to the contact zone with the Adriatic lower crust protruding northwards the European crust as interpreted by Schmid & Kissling (2000) (see lower inset Fig. 11). We note the receiver function image appears to reveal deep-seated lower-crust and upper-mantle features that had not been identified previously by active source experiments.

© 2008 The Authors, *GJI*, **173,** 249–264
Journal compilation © 2008 RAS

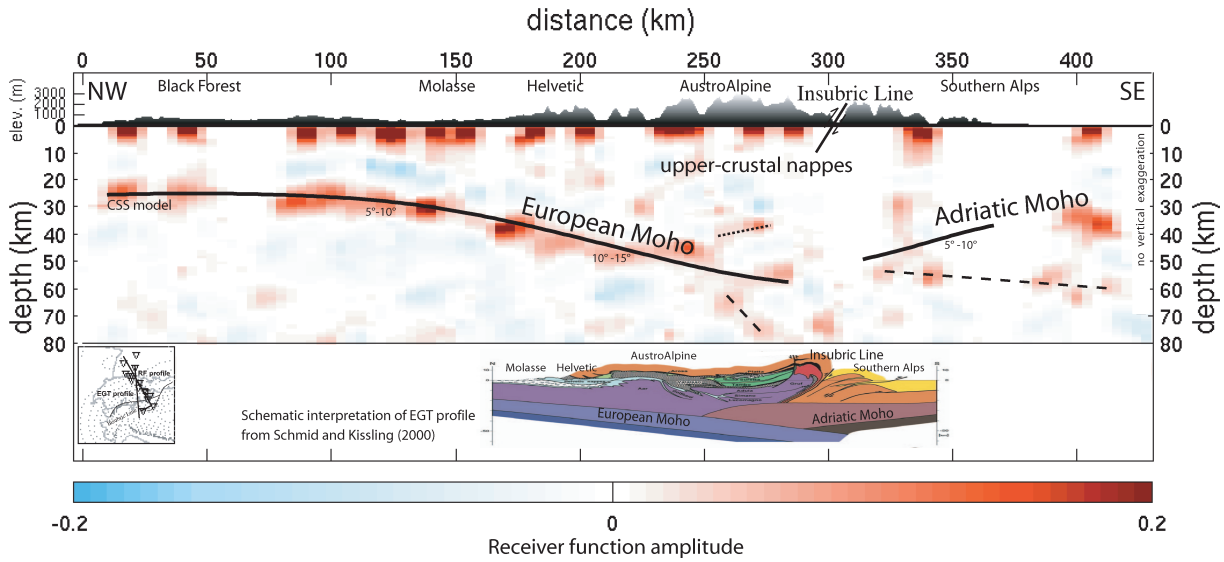

Figure 11. Common conversion point receiver function back-projected along a NW (left-hand side) to SE (right-hand side) profile (lower-left-hand side inset) through the eastern Central Alps. Thick solid lines are Moho depths from the CSS model that match the depth of the strongest receiver function amplitudes (red) fairly well. Although the southern part of the section ($x > 300$ km) is poorly constrained due to lack of adequate station coverage, a distinct offset in the continuity of European Moho beneath the location of the Insubric Line ($x = 300$ km) marks the transition from the SE dipping European Moho to the possibly NE dipping Adriatic Moho. Two segments (dashed lines) may be interpreted as European crustal detachments. Another area of strong amplitude (hatched line) lying above the European Moho at depth of 40 km ($x = 260$ km), may be attributed to the Adriatic lower-crust protruding the European crust as suggested from the interpretation of the EGT profile from Schmid & Kissling (2000, bottom plot).

3.2 Poisson's ratio with respect to tectonic units

The obtained crustal average Vp/Vs ratios from dip-corrected H–κ analysis and from combining Ps-times with CSS Moho depths are given in Table 1. Our preferred station Vp/Vs ratios are weighted means from both approaches when available. The results, within their uncertainties, are consistent (except WIMIS) and mean Vp/Vs ranges from 1.60 (LLS) to 2.00 (RORO). Our relatively large mean uncertainty (± 0.08) represents a conservative estimate with H–κ uncertainties slightly smaller (± 0.06) than from Ps-times (± 0.09). The first approach suffers mainly from limited bandwidth of teleseismic data and arrival time variability of reverberated phased, while the second is affected by the large variability in the data quality of the seismic profiles. To compensate for large station uncertainties and to minimize local variations, we produced average Vp/Vs ratios for tectonic units by binning stations within one unit. Inspired by a study for the Australian continent (Chevrot & van der Hilst 2000), we show Vp/Vs ratio variation between tectonic units as function of Moho depth (Fig. 12) and location along the Alpine chain (Fig. 13). Compared to Australia, our study area is smaller, tectonically younger and more complex, but we can observe clear trends. The crustal averages cannot resolve composition and structure of the crust in detail, but rather provide insight into overall compositional differences and variations in crustal architecture due to upper- versus lower-crust thickening as response to Alpine collision tectonics. In the next sections, we discuss these behaviours in terms of Poisson's ratio more meaningful than Vp/Vs ratio when considering lithologies.

3.2.1 *Variscan basement*

Stations in the Vosges and Black Forest (ECH, BFO and KIZ) have a Moho at 25 km depth consistent with the CSS model (Fig. 10) and previous receiver function studies (Kind *et al.* 1995; Geissler *et al.* 2005). The weighted average Poisson's ratio is equal to 0.24 ($Vp/Vs = 1.72$; Fig. 12). The low value is probably due to high quartz content in the granitic-gneiss basement that outcrops in the area and presence of a P-wave low-velocity zone associated with relatively high S-wave velocities at mid-crust depths deduced from seismic refraction profiles (Holbrook *et al.* 1988). Holbrook *et al.* (1988) interpreted the anticorrelated velocity variation by the presence of fluids at low pore pressure that had been liberated during the mid-Eocene rifting of the Rhinegraben.

3.2.2 *Mesozoic cover*

Stations within the larger area of the Mesozoic cover (Fig. 12) have a Moho depth in the range [24–31 km] (Fig. 10). The average Poisson's ratio of 0.24–0.25 ($Vp/Vs = 1.72$–1.73, Fig. 12) is consistent with previous results in southwest Germany (Holbrook *et al*. 1988). For northern Switzerland, Deichmann & Rybach (1989) estimated a Poisson's ratio of 0.23–0.24 from a Wadati diagram analysis of earthquakes in the 6–30 km depth range; their slightly lower value possibly reflects undersampling of mafic lower crust and of regions with thick, 2–3 km superficial limestone characterized by a high Poisson's ratio from high calcite content (Domenico 1984).

3.2.3 *Molasse basin*

Beneath the Molasse Basin, the Moho is [26–31 km] deep (Fig. 10) consistent with the CSS model and receiver function studies (Kind *et al.* 1995; Geissler *et al.* 2005). The Poisson's ratio is in the range 0.25–0.26 ($Vp/Vs = 1.74$–1.75) with a rather large uncertainty (± 0.02) due to the extreme value of 0.30 ($Vp/Vs = 1.87$) for station FUR in the Bavarian Molasse contrasting with values found for stations in the Swiss Molasse (less than 0.26). This is probably due to the relatively thin Molasse layer in Switzerland (Pfiffner *et al.* 1997b) raising the ratio only slightly compared to

Table 1. Results of Moho depth and *Vp*/*Vs* ratio from *H*–κ technique ('H_RF', 'κ_RF') and from combining receiver function and CSS data ('κ_CSS'). 'Nb. RF' is the number of receiver functions. 'C_H_RF' and 'C_κ _RF' refer to the dip-corrections applied, respectively, to the Moho depth and *Vp*/*Vs* values resulting from the *H*–κ technique. 'H_CSS' are depths from the CSS model; values marked by an '∗' are from Thouvenot *et al.* (2007) for stations with ill-defined CSS depth, for these, we assigned ±4 km uncertainty leading to estimate *Vp*/*Vs* uncertainty. Crosses in column 'H_RF' are depths determined using *Ps* time and a *Vp*/*Vs* ratio of 1.75 ± 0.1. The last column shows the weighted average *Vp*/*Vs* ratio ('Mean κ') calculated from 'κ_RF' and 'κ_CSS'.

Station	Latitude (°)	Longitude (°)	Nb. RF	C_H_RF (km)	H_RF (km)	H_CSS (km)	C_κ_RF	κ_RF	κ_CSS	Mean κ
ACB	47.58	8.25	32	0.0	27 ± 4	28 ± 5	−0.01	1.71 ± 0.05	1.71 ± 0.09	1.71 ± 0.07
AIGLE	46.34	6.95	90	2.5	38 ± 5	37 ± 6	−0.05	1.67 ± 0.09	1.62 ± 0.07	1.64 ± 0.08
BALST	47.34	7.69	91	0.0	27 ± 4	29 ± 12	−0.01	1.73 ± 0.05	1.68 ± 0.21	1.72 ± 0.13
BERNI	46.41	10.02	90		53 ± 7$^+$	54 ± 6		1.75 ± 0.06		1.75 ± 0.06
BFO	48.33	8.33	112	0.0	26 ± 4	25 ± 8	0.00	1.68 ± 0.05	1.69 ± 0.16	1.68 ± 0.10
BNALP	46.87	8.43	83	4.0	37 ± 5	38 ± 4	−0.08	1.74 ± 0.07	1.72 ± 0.05	1.72 ± 0.06
BNI	45.05	6.68	66	4.0	53 ± 5	53 ± 4*	−0.01	1.72 ± 0.05	1.68 ± 0.04	1.70 ± 0.04
BOURR	47.39	7.18	72	0.0	27 ± 4	27 ± 8	0.00	1.76 ± 0.05	1.77 ± 0.16	1.77 ± 0.10
BRANT	46.94	6.47	32	0.0	28 ± 4	29 ± 6	−0.01	1.87 ± 0.06	1.86 ± 0.13	1.87 ± 0.10
CALF	43.75	6.92	59		31 ± 4$^+$	34 ± 12		1.70 ± 0.18		1.70 ± 0.18
DAVA	47.28	9.88	102	2.5	39 ± 4	38 ± 8	−0.05	1.71 ± 0.06	1.72 ± 0.11	1.71 ± 0.08
DAVOX	46.78	9.88	65		50 ± 7$^+$	49 ± 5		1.79 ± 0.06		1.79 ± 0.06
DIX	46.08	7.41	79		46 ± 6$^+$	46 ± 8		1.76 ± 0.10		1.76 ± 0.10
DOI	44.50	7.25	21	1.5	53 ± 5	49 ± 6	−0.03	1.96 ± 0.07	2.03 ± 0.08	1.99 ± 0.07
ECH	48.22	7.16	72	0.0	25 ± 4	25 ± 6	0.00	1.71 ± 0.05	1.73 ± 0.14	1.72 ± 0.09
EMV	46.06	6.90	89	3.0	39 ± 4	40 ± 5	−0.05	1.79 ± 0.06	1.77 ± 0.07	1.78 ± 0.06
ESCA	43.83	7.37	20		30 ± 4$^+$	36 ± 12		1.67 ± 0.16		1.67 ± 0.16
FLACH	47.57	8.57	47	0.5	27 ± 4	29 ± 5	−0.02	1.75 ± 0.05	1.72 ± 0.09	1.74 ± 0.07
FUORN	46.62	10.26	103		58 ± 8$^+$	52 ± 8		1.86 ± 0.09		1.86 ± 0.09
FUR	48.16	11.28	70	0.0	28 ± 4	31 ± 5	−0.01	1.91 ± 0.05	1.82 ± 0.09	1.88 ± 0.07
GIMEL	46.53	6.27	59	1.0	29 ± 4	32 ± 6	−0.02	1.72 ± 0.07	1.65 ± 0.10	1.69 ± 0.08
GRYON	46.25	7.11	45	2.5	39 ± 4	40 ± 5	−0.05	1.72 ± 0.06	1.69 ± 0.06	1.71 ± 0.06
GUT	48.07	9.11	46		27 ± 4$^+$	27 ± 4		1.74 ± 0.08		1.74 ± 0.08
HASLI	46.76	8.15	105	3.5	40 ± 4	38 ± 5	−0.07	1.67 ± 0.05	1.73 ± 0.07	1.70 ± 0.06
KAMOR	47.29	9.49	107	2.0	37 ± 4	37 ± 3	−0.04	1.67 ± 0.05	1.68 ± 0.05	1.67 ± 0.05
KIZ	47.96	7.92	31	0.0	24 ± 4	25 ± 6	0.00	1.73 ± 0.06	1.69 ± 0.12	1.72 ± 0.09
LKBD	46.39	7.63	22	3.5	41 ± 4	42 ± 4	−0.06	1.71 ± 0.06	1.69 ± 0.05	1.70 ± 0.06
LKBD(5s)	46.39	7.63	29	3.5	41 ± 5	42 ± 4	−0.06	1.72 ± 0.09	1.71 ± 0.06	1.71 ± 0.07
LLS	46.85	9.01	132	3.5	43 ± 4	43 ± 6	−0.06	1.59 ± 0.05	1.62 ± 0.07	1.60 ± 0.06
MABI	46.05	10.51	23		38 ± 5$^+$	44 ± 5		1.64 ± 0.05		1.64 ± 0.05
MDGS	47.31	6.39	19		27 ± 4$^+$	27 ± 5		1.72 ± 0.10		1.72 ± 0.10
MDI	45.77	9.72	29		33 ± 4$^+$	37 ± 5		1.67 ± 0.07		1.67 ± 0.07
MELS	47.05	9.38	38	2.5	41 ± 4	41 ± 5	−0.05	1.67 ± 0.05	1.66 ± 0.06	1.66 ± 0.05
MMK	46.05	7.96	85		51 ± 7$^+$	53 ± 8		1.72 ± 0.08		1.72 ± 0.08
MUGIO	45.92	9.04	56		35 ± 5$^+$	35 ± 4		1.75 ± 0.06		1.75 ± 0.06
MUO	46.97	8.64	97		34 ± 5$^+$	38 ± 5		1.67 ± 0.06		1.67 ± 0.06
OG05	46.04	5.46	16	0.5	31 ± 5	30 ± 5	−0.01	1.74 ± 0.06	1.74 ± 0.09	1.74 ± 0.07
OGAG	44.79	6.54	15		43 ± 6$^+$	50 ± 4∗		1.63 ± 0.04		1.63 ± 0.04
OGDI	44.11	6.22	14		37 ± 5$^+$	34 ± 4∗		1.74 ± 0.07		1.74 ± 0.07
PLONS	47.05	9.38	107	2.5	40 ± 4	41 ± 5	−0.05	1.66 ± 0.05	1.66 ± 0.06	1.66 ± 0.05
RORO	44.11	8.07	17	0.0	23 ± 4	23 ± 6	0.00	1.99 ± 0.10	2.00 ± 0.18	2.00 ± 0.14
RSL	45.69	6.62	32	2.0	38 ± 5	41 ± 8	−0.03	1.90 ± 0.07	1.79 ± 0.11	1.86 ± 0.09
SAOF	43.99	7.55	88		37 ± 5$^+$	38 ± 12		1.76 ± 0.17		1.76 ± 0.17
SENIN	46.36	7.30	64	2.5	41 ± 4	39 ± 6	−0.05	1.66 ± 0.06	1.68 ± 0.08	1.67 ± 0.07
SLE	47.77	8.49	73	0.0	27 ± 4	27 ± 5	0.00	1.67 ± 0.05	1.67 ± 0.09	1.67 ± 0.07
STEIN	47.67	8.87	30	0.0	26 ± 5	29 ± 6	−0.01	1.80 ± 0.07	1.75 ± 0.12	1.78 ± 0.10
STET	44.26	6.93	80		44 ± 6$^+$	41 ± 12		1.78 ± 0.16		1.78 ± 0.16
STU	48.77	9.20	122	0.0	24 ± 4	26 ± 3	0.00	1.72 ± 0.05	1.67 ± 0.07	1.70 ± 0.06
SULZ	47.53	8.11	82	0.5	25 ± 4	28 ± 6	−0.02	1.78 ± 0.06	1.72 ± 0.12	1.76 ± 0.09
TORNY	46.77	6.96	58	1.0	31 ± 4	32 ± 8	−0.02	1.76 ± 0.05	1.74 ± 0.13	1.76 ± 0.09
TRULL	47.65	8.68	43	0.0	28 ± 4	28 ± 5	−0.01	1.68 ± 0.05	1.69 ± 0.09	1.68 ± 0.07
VDL	46.48	9.45	113		49 ± 6$^+$	53 ± 6		1.69 ± 0.06		1.69 ± 0.06
WEIN	47.53	8.98	37	1.5	30 ± 4	31 ± 6	−0.04	1.75 ± 0.05	1.74 ± 0.11	1.75 ± 0.08
WILA	47.41	8.91	63	2.0	32 ± 4	32 ± 5	−0.05	1.70 ± 0.05	1.70 ± 0.08	1.70 ± 0.07
WIMIS	46.67	7.62	51	2.5	40 ± 4	37 ± 4	−0.05	1.54 ± 0.05	1.67 ± 0.05	1.60 ± 0.05
WTTA	47.26	11.64	67	4.5	51 ± 5	45 ± 6	−0.07	1.79 ± 0.07	1.88 ± 0.09	1.83 ± 0.08
ZUR	47.37	8.58	74	1.5	30 ± 4	31 ± 5	−0.04	1.72 ± 0.04	1.71 ± 0.08	1.72 ± 0.06

© 2008 The Authors, *GJI*, **173,** 249–264
Journal compilation © 2008 RAS

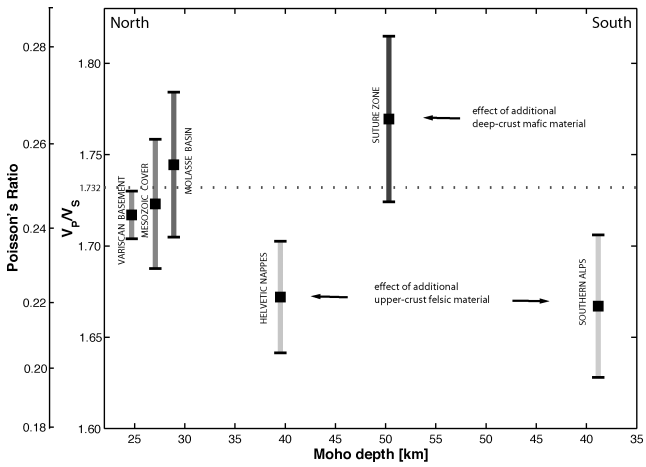

Figure 12. Distribution of Poisson's (and *Vp*/*Vs*) ratios (solid squares) and their standard deviation as function of Moho depth for each tectonic unit (vertically oriented text). The reference value of 0.25 (1.732) is shown as a thin dashed horizontal line. Although standard deviations are large, we recognize distinct behaviours with low values for the Helvetic and Southern Alps versus a high value for the suture zone region reflecting additional felsic and mafic material, respectively. See text for further discussion.

5–6-km-thick sediments of the Bavarian Molasse (Thomas *et al.* 2006) that cause the Poisson's ratio to rise to 0.30, a value confirming previous results (Geissler *et al.* 2005).

3.2.4 Helvetic-Dauphiné nappes

The Helvetic nappes are characterized by thick-layered stacks of upper-crustal nappes and rapid lithology changes with depth and within the unit (Maurer & Ansorge 1992). Nevertheless, we observe consistently low Poisson's ratios (0.22, $Vp/Vs = 1.68$, Figs 12 and 13) due to accumulation of upper-crustal deformed cover nappes. Our average is lower than the 0.25-value obtained from a refraction profile (Maurer & Ansorge 1992) sampling the Molasse-Helvetic front. We noticed that the two westernmost stations (EMV, RSL) of the unit show significantly larger values (0.27 and 0.29, respectively) than the others, and therefore, excluded them from average Poisson's ratio calculation as well as stations in the Western Alps whose Poisson's ratio uncertainties are relatively large due to ill-constrained Moho depths from the CSS model (Fig. 2).

3.2.5 Penninic nappes

The diverse Penninic unit consists of the PréAlpes nappes, the Briançonnais Terrane and the Piemont-Liguria domain each with different palaeogeographic origin and lithology (Fig. 1). The diversity is reflected in the Poisson's ratio results requiring detailed description. In the PréAlpes, stations WIMIS and AIGLE exhibit a very low Poisson's ratio (0.20, $Vp/Vs = 1.63$). The PréAlpes consist of a thin low-grade metamorphic sediment cover detached from the basement of the Briançonnais microcontinent and transported northward on top of Helvetic nappes and the Molasse during early stages of the Alpine Tertiary collision. Due to upper-crustal nappes accumulation, the Poisson's ratio is low and consistent with the ratio found for the Helvetic nappes. Probably for similar reasons, a low value of 0.22 is found for the Briançonnais Terrane of the Western Alps at stations BNI and OGAG. These low Poisson's ratios contrast with high values for RSL and EMV located further north in the External

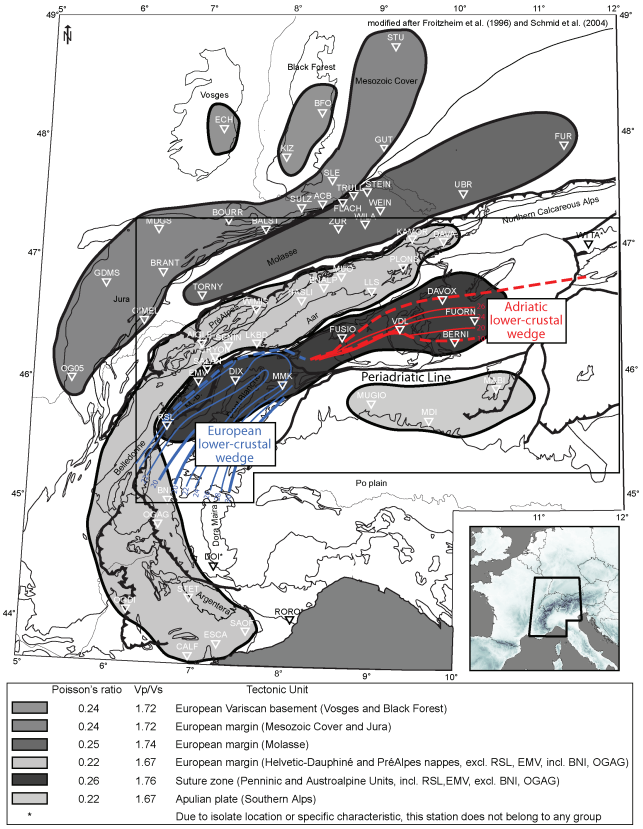

Figure 13. Compilation of Poisson's ratio results projected on a map of the Western–Central Alps with main tectonic units as in Fig. 1 (background contour lines). Grey shading (as in Fig. 12) indicates the spatial extent of tectonic units (as covered by our stations) and illustrates their geographical distribution and relation. Seismic stations are shown as inverted triangles. Outlines of the European (blue) and Adriatic (red) lower-crustal wedges are plotted after Schmid & Kissling (2000; their Fig. 5) with small numbers denoting depth to top of wedge. Location of indenting wedges agrees fairly well with area marked by a high Poisson's ratio (darker shaded area) representing thickened mafic lower crust in the Northern Western Alps and in the core of the Central Alps.

Crystalline Massif. The Poisson's ratio remains high further east in the Penninic nappes of Switzerland but progressively decreases from RSL (0.29, $Vp/Vs = 1.86$) towards the Central Alps (VDL 0.23, $Vp/Vs = 1.69$). In the southernmost part of the Penninic unit, just northeast of the Argentera massif (Fig. 13), DOI is located at the border between the ophiolites of the former Piemont-Liguria Ocean and the internal Dora Maira massif. A strong *Ps* phase at 7.5 s and a *PpPs* phase at 22.0 s (Fig. 8) lead to a Poisson's ratio of 0.33 ($Vp/Vs = 1.99$), which is probably a combined effect of a small amount of remnant oceanic crust and the dominant presence of ultramafic rocks of the Ivrea body as shown by tomography and gravity data (Paul *et al.* 2001; Vernant *et al.* 2002). RORO to the southeast is our only station above the 23 km shallow Ligurian Moho. RORO has a high Poisson's ratio like DOI; in this case due to a large amount of oceanic remnant material from the former Piemont-Liguria Ocean (Seno *et al.* 2005).

3.2.6 Austroalpine nappes

The Austroalpine nappes are composed of a stack of various crystalline nappes from Adriatic origin and cover slices of both Adriatic

and European origins until the underthrusted European basement is reached at about 15 km depth (Bleibinhaus & Gebrande 2006). For the Austrian station WTTA, we found a Poisson's ratio of almost 0.29 ($Vp/Vs = 1.83$; Table 1). For a site about 30 km east of WTTA, Geissler *et al.* (2005) also found a high ratio of 0.30, though their result is based on fewer receiver functions. A high Poisson's ratio (0.25–0.30) was found in the shallow part of the Northern Calcareous Alps (Zschau & Koschyk 1976), the northern rim of the Austroalpine nappes (Fig. 1), probably due to the dolomite-limestone layer in the uppermost 6 km. In the framework of the TRANSALP project (TRANSALP Working group 2002), Kummerow *et al.* (2004) imaged the crustal structure along a dense north–south receiver function profile a few kilometres east of WTTA. Their Moho depth of 45–50 km is slightly shallower than our value (51 ± 5 km), and their Poisson's ratio of 0.25 ($Vp/Vs = 1.73$) is significantly lower. Kummerow *et al.* (2004) were mainly interested in crustal imaging and we suspect their Poisson's ratio reflects a mean value over the 300-km-long profile rather than a local value such as ours. Nevertheless, considering WTTA's isolated location, we did not include it in any group presented in Figs 12 and 13. For the Austroalpine nappes of Switzerland, about 200 km west of WTTA, for stations DAVOX and FUORN, Poisson's ratios remain high (0.27, $Vp/Vs = 1.79$ and 0.29, $Vp/Vs = 1.86$, respectively). The nappes' southernmost station BERNI is located only a few kilometres north of the Insubric Line and shows an intermediate Poisson's ratio 0.25–0.26 ($Vp/Vs = 1.75$) slightly smaller than other stations in the Austroalpine nappes.

3.2.7 Southern Alps

South of the Insubric Line, the stations MUGIO, MDI and MABI are located in the cover nappes of the Southern Alps. The average Poisson's ratio is low (0.22) similar to the value for the Helvetic nappes (Fig. 12). However, the average is based on only three stations each with relatively low data quality and the reliability of our estimate is currently relatively low.

3.3 Discussion

The main contribution of our study is documentation of Poisson's ratio variations that are geographically correlated along the Alpine belt. Our discussion thus focuses on this important parameter reflecting variations in overall structural composition of different tectonic units. The Poisson's ratio in the Alpine Foreland (Figs 12 and 13, Variscan basement, Mesozoic cover and Molasse basin units), overall, is close to the 0.25 value found globally for Mesozoic–Cenozoic orogenic belts (Zandt & Ammon 1995). In the Alps proper, the Poisson's ratio decreases to 0.22 in the Helvetic and Southern Alps nappes as a consequence of intense upper-crustal deformation during collision processes piling thick stacks of primarily felsic material on top of each other. Near the suture zone, consisting of Penninic and Austroalpine units, we observe a significant increase of the mean Poisson's ratio to 0.26. The increase implies a different tectonic process is responsible for increasing the ratio of mafic-to-felsic material in the crustal column. A logic choice, based on crust and upper-mantle lithologies and their Poisson's ratio (see Christensen 1996), is to assume addition of mafic material at deep crustal levels beneath the suture. Reviewing previous interpretations and geophysical data, Schmid & Kissling (2000) suggested the core of the Alpine crust consists of an indenting wedge doubling the lower-crust thickness. They proposed the wedge is likely to consist of European lower-crust in the Western Alps and of Adriatic origin in the Central Alps while ruling out a mantle origin.

The Poisson's ratios provide another means to test whether the indenting wedge is of crust or mantle origin. The lower crust, due to a higher plagioclase content of its main constituents, the high-grade lithologic facies mafic granulite, eclogite and garnet granulite (Christensen & Mooney 1995), has a higher Poisson's ratio of about 0.28 than normal upper-mantle peridotite (0.25–0.26, Christensen 1996). However, considering Alpine tectonics, its upper-mantle may not consist primarily of peridotite. Presence of relicts of subducted crustal material or a certain degree of serpentinization (Rossi *et al.* 2006) may lead to a broad range of upper-mantle Poisson's ratios complicating discrimination. Considering DOI samples Ivrea mantle material (Paul *et al.* 2001; Vernant *et al.* 2002), it seems likely that Adriatic upper mantle may also have a high Poisson's ratio (∼0.33) larger than ratios found for stations RSL, EMV, DIX and MMK in the Northern Western Alps (∼0.27), which sample the wedge (Fig. 13). It thus seems more likely that the wedge, at least south of the Rhone-Simplon Line, is not mantle material as originally suggested by Nicolas *et al.* (1990a,b) and Roure *et al.* (1990b) but rather European lower-crust as suggested by Schmid *et al.* (1996), Roure *et al.* (1996) and recently Schmid & Kissling (2000). Another important observation consistent with a European lower-crust indenter is a progressive west-to-east decrease in Poisson's ratio from about 0.29 at RSL to 0.24 at MMK and 0.23 at VDL suggesting a thinning of the lower-crust wedge towards the Central Alps. The low ratios possibly mark the transition from European to Adriatic lower wedge south of the Aar Massif in the vicinity of FUSIO (Fig. 13) as suggested by Schmid & Kissling (2000).

In the eastern Central Alps, the Poisson's ratio increases again suggesting thickening of an Adriatic lower-crust wedge eastwards. At DAVOX, with well-constrained CSS Moho, we obtained 0.27 and for FUORN to the southwest 0.29. For FUORN, no quality CSS data exist and the ratio is less well resolved; however, a Moho depth in excess of 60 km is needed to reduce the ratio to 0.25, unlikely considering the Alpine topographic load is already regarded as overcompensated (Kissling 1980; Klingelé & Kissling 1982). The high ratios seem reliable and are consistent with the location of the thickest part of the Adriatic lower-crust wedge (Fig. 13) mapped by Schmid & Kissling (2000). We note a lower ratio at BERNI (0.26) is consistent with the proposed southern limit of the wedge proposed by Schmid & Kissling (2000).

A continuation of the mafic European lower crust wedge into the Western Alps much south of station RSL seems unlikely based on low Poisson's ratios observed for sites OGAG and BNI (0.20 and 0.23, respectively) in the Briançonnais of the Western Alps. This implies a disconnection of deep crustal structure in the Western Alps that seems to coincide roughly with the bend in the Alpine chain. Differences in deep crustal structure along the Western Alps had already been observed from wide-angle seismic data (ECORS-CROP deep seismic sounding group 1989; Thouvenot *et al.* 2007). The Poisson's ratios obtained here remain averaged over the whole crust and further analysis is required to place further constrain on the nature and the amount of the Alpine indentation.

4 CONCLUSION

This study presents first results of receiver function analysis in the Western–Central Alps exploiting about 6 yr of high-quality data from a 61 station seismic network covering the orogen rather uniformly and densely. Our focus is on average crustal structure and we report well-constrained Moho depths augmenting CSS depths and first orogen-scale crustal Poisson's ratios for lithological interpretation. Estimates are mainly based on the H–κ technique (Zhu &

© 2008 The Authors, *GJI*, **173,** 249–264
Journal compilation © 2008 RAS

Kanamori 2000). Using synthetic receiver functions, we show the importance of a dipping Moho on the results of H–κ technique. We improve the usual approach including corrections to minimize dip-induced bias and reconcile receiver function and controlled-source seismology depths. The receiver functions image a gently southeast dipping European Moho beneath the northern Alpine foreland ($H \leq$ 40 km). The dip increases from 5–10° to about 15° towards the suture zone where the Moho depth reaches a maximum value of about 55 km. South of the Periadriatic Line, the Adriatic Moho reaches a depth of about 40–45 km possibly dipping north–northeast. In the suture zone, we observe several coherent conversions from 40 to 70 km depth not previously documented. We also obtain Moho depths of 30–53 km for the previously ill-constrained southern part of the Western Alps consistent with recent refraction results (Thouvenot *et al.* 2007). We present the first large-scale attempt to determine average crustal Poisson's ratios in the Alpine belt. Binning individual station values for major tectonic units, we find a remarkable difference between units probably directly related to gross crustal composition. Units in the Alpine foreland show a normal Poisson's ratio near 0.25. The Helvetic nappes and Southern Alps, forming the distal part of the orogen, have a low average ratio of 0.22, which we attribute to upper-crustal thickening. The Penninic and Austroalpine units near the suture zone have a large ratio of 0.26–0.27, which supports the model presented by Schmid & Kissling (2000) that thickening in the Alpine core is due to a European lower-crust indenter in the Northern Western Alps that pinches out eastwards where it is replaced by thickened Adriatic lower crust. A European lower-crust origin for the indenter in the Western Alps is supported by low Poissons ratio's for sites in the Northern Western Alps compared to the high ratio at station DOI, which samples the mafic Ivrea material of Adriatic mantle origin. Low ratios in the southern Western Alps, compared to sites in the north, imply a discontinuity of the deep crustal structure of the Western Alps.

5 ACKNOWLEDGMENTS

We thank the Swiss Seismological Service for providing data from the SDS-Net and for operating seven temporary broad-band stations in France and in Germany in collaboration with the Laboratoire de Géophysique Interne et Tectonophysique, Observatoire de Grenoble and the Erdebebendienst des Landesamtes für Geologie, Rohstoffe und Bergau Baden Württemberg in Freiburg. We gratefully acknowledge the GEOSCOPE, GIS-RAP, GRSN, INGV, MedNet, RosAlp, RSNI, TGRS and ZAMG networks for providing high-quality broad-band data. We also thank Andrew Frederiksen for providing the forward modelling code. The manuscript profited from constructive comments by John Cassidy and one anonymous reviewer. This research was supported by Swiss National Fund grant 2100-068158. This is contribution 1514 of the Institute of Geophysics, ETH Zürich.

REFERENCES

Ammon, C.J., 1991. The isolation of receiver effects from teleseismic P waveforms, *Bull. seism. Soc. Am.,* **81,** 2504–2510.

Ammon, C.J., Randall, G.E. & Zandt, G., 1990. On the Nonuniqueness of Receiver Function Inversions, *J. Geophys. Res.-Solid Earth Planets,* **95,** 15 303–15 318.

Baer, M. et al., 2001. Earthquakes in Switzerland and surrounding regions during 2000, *Eclogae Geologicae Helvetiae,* **94,** 253–264.

Baumann, M., 1994. Three-dimensional modeling of the crust-mantle boundary in the Alpine region, *PhD thesis*, No. 10772, ETHZ, Zürich.

Bayer, R., Carozzo, M.T., Lanza, R., Miletto, M. & Rey, D., 1989. Gravity modelling along the ECORS-CROP vertical seismic reflection profile through the Western Alps, *Tectonophysics,* **162,** 203–218.

Bernoulli, D., Heitzmann, P. & Zingg, A., 1990. Central and southern Alps in southern Switzerland: tectonic evolution and first results of reflection seismics, in *Deep Structure of the Alps,* pp. 289–302, eds Roure, F., Heitzmann, P. & Polino, R., Mémoires de la Société Géologique de France, Paris, 156; Mémoires de la Société Géologique suisse, Zürich, 1; Volume speciale Società Geologica Italiana, Roma, 1990, 1.

Bertrand, E. & Deschamps, A., 2000. Lithospheric structure of the southern French Alps inferred from broadband analysis, *Phys. Earth planet. Inter.,* **122,** 79–102.

Bleibinhaus, F. & Gebrande, H., 2006. Crustal structure of the Eastern Alps along the TRANSALP profile from wide-angle seismic tomography, *Tectonophysics,* **414,** 51–69.

Blundell, D., Freeman, R. & Müller, S., eds, 1992. *A Continent Revealed: The European Geotraverse,* pp. 275, Cambridge University Press, Cambridge.

Burdick, L.J. & Langston, C.A., 1977. Modeling crustal structure through use of converted phases in teleseismic body-wave forms, *Bull. seism. Soc. Am.,* **67,** 677–691.

Cassidy, J.F., 1992. Numerical experiments in broad-band receiver function-analysis, *Bull. seism. Soc. Am.,* **82,** 1453–1474.

Chevrot, S. & van der Hilst, R.D., 2000. The Poisson ratio of the Australian crust: geological and geophysical implications, *Earth planet. Sci. Lett.,* **183,** 121–132.

Christensen, N.I., 1996. Poisson's ratio and crustal seismology, *J. Geophys. Res.-Solid Earth,* **101,** 3139–3156.

Christensen, N.I. & Mooney, W.D., 1995. Seismic velocity structure and composition of the continental-crust—a global view, *J. Geophys. Res.-Solid Earth,* **100,** 9761–9788.

Deichmann, N. & Rybach, L., 1989. Earthquakes and temperatures in the lower crust below the northern Alpine foreland of Switzerland, in *Properties and Processes of the Lower Crust,* Vol. 6, pp. 197–213, eds Mereu, R.F., Mueller, St. & Fountain, D., Am. Geophys. Union, Geophysical Monograph 51, IUGG.

Diehl, T., Ritter, J.R.R. & the CALIXTO Group, 2005. The crustal structure beneath SE Romania from teleseismic receiver functions, *Geophys. J. Int.,* **163,** 238–251.

Di Stefano, R., Chiarabba, C., Lucente, F. & Amato, A., 1999. Crustal and uppermost mantle structure in Italy from the inversion of *P*-wave arrival times: geodynamic implications, *Geophys. J. Int.,* **139,** 483–498.

Domenico, S.N., 1984. Rock lithology and porosity determination from shear and compressional wave velocity, *Geophysics,* **49,** 1188–1195.

Dueker, K.G. & Sheehan, A.F., 1997. Mantle discontinuity structure from midpoint stacks of converted P to S waves across the Yellowstone hotspot track, *J. Geophys. Res.-Solid Earth,* **102,** 8313–8327.

Dugda, M.T., Nyblade, A.A., Julià, J., Langston, C.A., Ammon, C.J. & Simiyu, S., 2005. Crustal structure in Ethiopia and Kenya from receiver function analysis: implications for rift development in eastern Africa, *J. Geophys. Res.-Solid Earth,* **110,** B01303, doi: 10.01310.01029/02004JB003065.

ECORS-CROP deep sounding seismic group, 1989. Mapping the Moho of the Western Alps by wide-angle reflection seismics, *Tectonophysics,* **162,** 193–202.

Efron, B. & Tibshirani, R., 1991. Statistical data analysis in the computer age, *Science,* **253,** 390–395.

Frederiksen, A.W. & Bostock, M.G., 2000. Modelling teleseismic waves in dipping anisotropic structures, *Geophys. J. Int.,* **141,** 401–412.

Frei, W., Heitzmann, P., Lehner, P., Muller, S., Olivier, R., Pfiffner, A., Steck, A. & Valasek, P., 1989. Geotraverses across the Swiss Alps, *Nature,* **340,** 544–548.

Froitzheim, N., Schmid, S.M. & Frey, M., 1996. Mesozoic paleogeography and the timing of eclogite-facies metamorphism in the Alps: a working hypothesis, *Eclogae Geologicae Helvetiae,* **89,** 81–110.

Geissler, W. et al., 2005. Seismic structure and location of a CO_2 source in the upper mantle of the western Eger (Ohře) Rift, central Europe, *Tectonics,* **24,** TC5001, doi:5010.1029/2004TC001672.

Giese, P. & Prodehl, C., 1977. *Main Features of Crustal Structure in the Alps in Explosion Seismology in Central Europe,* pp. 347–375, eds Giese, P., Prodelh, C. & Stein, A., Springer Verlag, Berlin.

Gilbert, H.J. & Sheehan, A.F., 2004. Images of crustal variations in the intermountain west, *J. Geophys. Res.-Solid Earth,* **109,** doi:10.10292003JB002730

Gilbert, H., Beck, S. & Zandt, G., 2006. Lithospheric and upper mantle structure of central Chile and Argentina, *Geophys. J. Int.,* **165,** 383–398.

Gurrola, H., Minster, J.B. & Owens, T., 1994. The use of velocity spectrum for stacking receiver functions and imaging upper-mantle discontinuities, *Geophys. J. Int.,* **117,** 427–440.

Gurrola, H., Baker, G.E. & Minster, J.B., 1995. Simultaneous time-domain deconvolution with application to the computation of receiver functions, *Geophys. J. Int.,* **120,** 537–543.

Holbrook, W.S., Gajewski, D., Krammer, A. & Prodehl, C., 1988. An interpretation of wide-angle compressional and shear-wave data in southwest Germany: Poisson's ratio and petrological implications, *J. Geophys. Res.-Solid Earth Planets,* **93,** 12 081–12 106.

Holliger, K. & Kissling, E., 1992. Gravity interpretation of a unified 2-D acoustic image of the central Alpine collision zone, *Geophys. J. Int.,* **111,** 213–225.

Husen, S., Kissling, E., Deichmann, N., Wiemer, S., Giardini, D. & Baer, M., 2003. Probabilistic earthquake location in complex three-dimensional velocity models: application to Switzerland, *J. Geophys. Res.-Solid Earth,* **108**(B2), 2077, doi:2010.1029/2002JB001778.

Julià, J. & Mejía, J., 2004. Thickness and Vp/Vs ratio variation in the Iberian Crust, *Geophys. J. Int.,* **156,** 59–72.

Kikuchi, M. & Kanamori, H., 1982. Inversion of complex body waves, *Bull. seism. Soc. Am.,* **72,** 491–506.

Kind, R., Kosarev, G.L. & Petersen, N.V., 1995. Receiver functions at the stations of the German Regional Seismic Network (GRSN), *Geophys. J. Int.,* **121,** 191–202.

Kind, R. et al., 2002. Seismic images of crust and upper mantle beneath Tibet: evidence for Eurasian plate subduction, *Science,* **298,** 1219–1221.

Kissling, E., 1980. Krustenaufbau und Isostasie in der Schweiz. *PhD thesis*, ETH, Zürich.

Klingelé, E. & Kissling, E., 1982. Zum Konzept der isostatischen Modelle in Gebirgen am Beispiel der Schweizer Alpen, Geodaetisch-geophysikalische Arbeiten in der Schweiz, *Schweizerische Geodaetische Kommission,* **35,** 3–36.

Kradolfer, U., 1996. AutoDRM—the first five years, *Seismol. Res. Lett.,* **67,** 30–33.

Kummerow, J., Kind, R., Oncken, O., Giese, P., Ryberg, T., Wylegalla, K., Scherbaum, F. & TRANSALP working group, 2004. A natural and controlled source seismic profile through the Eastern Alps: TRANSALP, *Earth planet. Sci. Lett.,* **225,** 115–129.

Langston, C.A., 1977. Corvallis, oregon, crustal and upper mantle receiver structure from teleseismic P-waves and S-waves, *Bull. seism. Soc. Am.,* **67,** 713–724.

Langston, C.A., 1979. Structure under Mount Rainier, Washington, inferred from teleseismic body waves, *J. Geophys. Res.,* **84,** 4749–4762.

Levin, V. & Park, J., 1997. P-SH conversions in a flat-layered medium with anisotropy of arbitrary orientation, *Geophys. J. Int.,* **131,** 253–266.

Ligorria, J.P. & Ammon, C.J., 1999. Iterative deconvolution and receiver-function estimation, *Bull. seism. Soc. Am.,* **89,** 1395–1400.

Maurer, H. & Ansorge, J., 1992. Crustal structure beneath the northern margin of the Swiss Alps, *Tectonophysics,* **207,** 165–181.

Mohsen, A., Hofstetter, R., Bock, G., Kind, R., Weber, M., Wylegalla, K., Rumpker, G. & Grp, D., 2005. A receiver function study across the Dead Sea Transform, *Geophys. J. Int.,* **160,** 948–960.

Nicolas, A., Polino, R., Hirn, A., Nicolich, R. & ECORS-CROP working group, 1990a. ECORS-CROP traverse and deep structure of the western Alps: a synthesis, in *Deep Structure of the Alps,* pp. 15–27, eds Roure, F., Heitzmann, P. & Polino, R., Mémoires de la Société Géologique de France, Paris, 156; Mémoires de la Société Géologique suisse, Zürich, 1; Volume speciale Società Geologica Italiana, Roma, 1.

Nicolas, A., Hirn, A., Nicolich, R. & Polino, R., 1990b. Lithospheric Wedging in the Western Alps Inferred from the Ecors-Crop Traverse, *Geology,* **18,** 587–590.

Owens, T. & Crosson, R., 1988. Shallow structure effects on broadband teleseismic *P* waveforms, *Bull. seism. Soc. Am.,* **78,** 96–108.

Ozacar, A. & Zandt, G., 2004. Crustal seismic anisotropy in central Tibet: implications for deformation style and flow in the crust, *Geophys. Res. Lett.,* **31,** L23601, doi:23610.21029/22004GL021096.

Park, J. & Levin, V., 2000. Receiver functions from multiple-taper spectral correlation estimates, *Bull. seism. Soc. Am.,* **90,** 1507–1520.

Paul, A., Cattaneo, M., Thouvenot, F., Spallarossa, D., Bethoux, N. & Frechet, J., 2001. A three-dimensional crustal velocity model of the south-western Alps from local earthquake tomography, *J. Geophys. Res.-Solid Earth,* **106,** 19 367–19 389.

Paulssen, H., Visser, J. & Nolet, G., 1993. The crustal structure from teleseismic P-wave coda. I: method, *Geophys. J. Int.,* **112,** 15–25.

Pedersen, H.A., Coutant, O., Deschamps, A., Soulage, M. & Cotte, N., 2003. Measuring surface wave phase velocities beneath small broad-band arrays: tests of an improved algorithm and application to the French Alps, *Geophys. J. Int.,* **154,** 903–912.

Pfiffner, O.A., Lehner, P., Heitzmann, P., Müller, S., & Steck, A., eds, 1997a. *Deep Structure of the Swiss Alps: Results from NRP 20,* pp. 380, Birkhäuser Verlag, Basel, Boston, Berlin.

Pfiffner, O.A., Erard, P.-F. & Stäuble, M., 1997b. Two cross sections through the Swiss Molasse Basin (lines E4 – E3, W1, W7 – W10), in *Deep Structure of the Swiss Alps – Results from NRP 20,* pp. 64–72, eds Pfiffner, O.A., Lehner, P., Heitzman, P.Z., Mueller, S. & Steck, A., Birkhaüser AG, Basel, 123.

Phinney, R.A., 1964. Structure of the Earth's crust from spectral behaviour of long-period body waves, *J. Geophys. Res.,* **69,** 2997–3017.

Rossi, G., Abers, G.A., Rondenay, S. & Christensen, D.H., 2006. Unusual mantle Poisson's ratio, subduction, and crustal structure in central Alaska, *J. Geophys. Res.-Solid Earth,* **111,** doi:10.1029/2005JB003956.

Roure, F., Heitzmann, P. & Polino, R., eds, 1990a. *Deep Structure of the Alps,* pp. 350, Mémoires de la Société Géologique de France, Paris, 156; Mémoires de la Société Géologique suisse, Zürich, 1; Volume speciale Società Geologica Italiana, Roma, 1.

Roure, F., Polino, R. & Nicolich, R., 1990b. Early Neogene deformation beneath the Po Plain, constraints on the post-collisional Alpine evolution, in *Deep Structure of the Alps,* pp. 309–322, eds Roure, F., Heitzmann, P. & Polino, R., Mémoires de la Société géologique de France, Paris.

Roure, F., Choukroune, P. & Polino, R., 1996. Deep seismic reflection data and new insights on the bulk geometry of mountain ranges, *Comptes Rendus De L'Academie Des Sciences,* **322,** 345–359.

Schmid, S.M. & Kissling, E., 2000. The arc of the western Alps in the light of geophysical data on deep crustal structure, *Tectonics,* **19,** 62–85.

Schmid, S.M., Pfiffner, O.A., Froitzheim, N., Schonborn, G. & Kissling, E., 1996. Geophysical-geological transect and tectonic evolution of the Swiss-Italian Alps, *Tectonics,* **15,** 1036–1064.

Schmid, S.M., Fugenschuh, B., Kissling, E. & Schuster, R., 2004. Tectonic map and overall architecture of the Alpine orogen, *Eclogae Geologicae Helvetiae,* **97,** 93–117.

Seno, S., Dallagiovanna, G. & Vanossi, M., 2005. A kinematic evolutionary model for the Penninic sector of the central Ligurian Alps, *Int. J. Earth Sci.,* **94,** 114–129.

Solarino, S., Kissling, E., Cattaneo, M. & Eva, C., 1997. Local earthquake tomography of the southern part of the Ivrea body, north-western Italy, *Eclogae Geologicae Helvetiae,* **90,** 357–364.

Steck, A., Epard, J.-L., Escher, A., Lehner, P., Marchant, R. & Masson, H., 1997. Geologic interpretation of the seismic profiles through western Switzerland: Rawil (W1), Val d'Anniviers (W2), Mattertal (W3), Zmutt-Zermatt-Findelen (W4) and Val de Bagnes (W5), in *Deep Structure of the Swiss Alps – Results from NRP 20,* pp. 123–138, eds Pfiffner, O.A., Lehner, P., Heitzman, P.Z., Mueller, S. & Steck, A., Birkhaüser AG, Basel.

Thouvenot, F., Paul, A., Fréchet, J., Béthoux, N., Jenatton, L. & Guiguet, R., 2007. Are there really superposed Mohos in the south-western Alps? New seismic data from fan-profiling reflections, *Geophys. J. Int.,* **170,** 1180–1194.

Thomas, R., Schwerd, K., Bram, K. & Fertig, J., 2006. Shallow high-resolution seismics and reprocessing of industry profiles in southern Bavaria: the Molasse and the northern Alpine front, *Tectonophysics,* **414,** 87–96.

TRANSALP Working Group, 2002. First deep seismic reflection images of the Eastern Alps reveal giant crustal wedges and transcrustal ramps, *Geophys. Res. Lett.*, **29**(10), doi:10.1029/2002GL014911., 29.

Vergne, J., Wittlinger, G., Hui, Q.A., Tapponnier, P., Poupinet, G., Mei, J., Herquel, G. & Paul, A., 2002. Seismic evidence for stepwise thickening of the crust across the NE Tibetan plateau, *Earth planet. Sci. Lett.,* **203,** 25–33.

Vernant, P., Masson, F., Bayer, R. & Paul, A., 2002. Sequential inversion of local earthquake traveltimes and gravity anomaly—the example of the western Alps, *Geophys. J. Int.,* **150,** 79–90.

Waldhauser, F., Kissling, E., Ansorge, J. & Mueller, S., 1998. Three-dimensional interface modelling with two-dimensional seismic data: the Alpine crust-mantle boundary, *Geophys. J. Int.,* **135,** 264–278.

Waldhauser, F., Lippitsch, R., Kissling, E. & Ansorge, J., 2002. High-resolution teleseismic tomography of upper-mantle structure using an a priori three-dimensional crustal model, *Geophys. J. Int.,* **150,** 403–414.

Wittlinger, G. *et al*., 2004. Teleseismic imaging of subducting lithosphere and Moho offsets beneath western Tibet, *Earth planet. Sci. Lett.,* **221,** 117–130.

Ye, S., Ansorge, J., Kissling, E. & Mueller, S., 1995. Crustal structure beneath the eastern Swiss Alps derived from seismic-refraction data, *Tectonophysics,* **242,** 199–221.

Zandt, G. & Ammon, C.J., 1995. Continental-crust composition constrained by measurements of crustal Poisson's ratio, *Nature,* **374,** 152–154.

Zandt, G., Myers, S.C. & Wallace, T.C., 1995. Crust and mantle structure across the basin and range Colorado Plateau boundary at 37-degrees-N latitude and implications for Cenozoic extensional mechanism, *J. Geophys. Res.-Solid Earth,* **100,** 10 529–10 548.

Zschau, J. & Koschyk, K., 1976. Results of a combined evaluation of longitudinal and transverse waves on a seismic profile along the northern margin of the Alps. in *Explosion Seismology in Central Europe,* pp. 332–338. eds Giese, P., Prodehl, C. and Stein, A., Springer Verlag, Berlin.

Zelt, B.C. & Ellis, R.M., 1999. Receiver-function studies in the Trans-Hudson Orogen, Saskatchewan, *Can. J. Earth Sci.,* **36,** 585–603.

Zhu, L.P. & Kanamori, H., 2000. Moho depth variation in southern California from teleseismic receiver functions, *J. Geophys. Res.-Solid Earth,* **105,** 2969–2980.

Zor, E., Sandvol, E., Gürbüz, C., Türkelli, N., Seber, D. & Barazangi, M., 2003. The crustal structure of the East Anatolian plateau (Turkey) from receiver functions, *Geophys. Res. Lett.,* **30**(24), 8044, doi:8010.1029/2003GL018192.

SUPPLEMENTARY MATERIAL

The following supplementary material is available for this article:

Figure S1. Stacked receiver functions for 57 stations providing results in alphabetical order. Station name is shown on top right-hand side of each trace. 'Nb. RF' is number of receiver functions in each stack; labels ending in 'baz' indicate only events from that backazimuth are included for maximal signal coherency. We give predicted arrival times of *Ps*, *PpPs* and *PsPs* + *PpSs* phases for stations with reliable reverberated phases allowing H–κ stacking and *Ps* times for other stations.

This material is available as part of the online article from: http://www.blackwell-synergy.com/doi/abs/10.1111/j.1365-246X.2006.03706.x (this link will take you to the article abstract).

Please note: Blackwell Publishing are not responsibe for the content or functionality of any supplementary materials supplied by the authors. Any queries (other than missing material) should be directed to the corresponding author for the article.